Direct numerical simulation of turbulent pipe flow using the lattice Boltzmann method

Cheng Peng [a], Nicholas Geneva [a], Zhaoli Guo [b], Lian-Ping Wang [a,b,∗]

[a] *Department of Mechanical Engineering, 126 Spencer Laboratory, University of Delaware, Newark, DE 19716-3140, USA*
[b] *State Key Laboratory of Coal Combustion, Huazhong University of Science and Technology, Wuhan, PR China*

ARTICLE INFO

ABSTRACT

In this paper, we present a first direct numerical simulation (DNS) of a turbulent pipe flow using the mesoscopic lattice Boltzmann method (LBM) on both a D3Q19 lattice grid and a D3Q27 lattice grid. DNS of turbulent pipe flows using LBM has never been reported previously, perhaps due to inaccuracy and numerical stability associated with the previous implementations of LBM in the presence of a curved solid surface. In fact, it was even speculated that the D3Q19 lattice might be inappropriate as a DNS tool for turbulent pipe flows. In this paper, we show, through careful implementation, accurate turbulent statistics can be obtained using both D3Q19 and D3Q27 lattice grids. In the simulation with D3Q19 lattice, a few problems related to the numerical stability of the simulation are exposed. Discussions and solutions for those problems are provided. The simulation with D3Q27 lattice, on the other hand, is found to be more stable than its D3Q19 counterpart. The resulting turbulent flow statistics at a friction Reynolds number of $Re_\tau = 180$ are compared systematically with both published experimental and other DNS results based on solving the Navier–Stokes equations. The comparisons cover the mean-flow profile, the r.m.s. velocity and vorticity profiles, the mean and r.m.s. pressure profiles, the velocity skewness and flatness, and spatial correlations and energy spectra of velocity and vorticity. Overall, we conclude that both D3Q19 and D3Q27 simulations yield accurate turbulent flow statistics. The use of the D3Q27 lattice is shown to suppress the weak secondary flow pattern in the mean flow due to numerical artifacts.

© 2017 Elsevier Inc. All rights reserved.

1. Introduction

Over the last two decades, the lattice Boltzmann method (LBM) has been rapidly developed into an alternative and viable computational fluid dynamics (CFD) method for simulating viscous fluid flows involving complex boundary geometries or moving fluid–solid/fluid–fluid interfaces [1]. Unlike conventional (macroscopic) CFD methods that are based on directly solving the Navier–Stokes (N–S) equations, LBM is a mesoscopic method that is governed by a discretized version of gas kinetic equation in which molecular distribution functions are relaxed locally and then propagated to their neighboring locations. Since only local data communication is needed in each time step, LBM is extremely suitable for large-scale simulations that require parallel computation using a large number of processors, *e.g.*, direct numerical simulations (DNS) of turbulent flows. Although still confined to relative low to moderate flow Reynolds (*Re*) numbers, DNS has been established as an

independent research tool to study the physics of turbulent flows. The data generated from DNS not only agrees well with experimental results, but often provides greater details and insights of the flow field to a degree that may be very difficult or impossible to achieve experimentally.

In recent years, the capabilities of LBM as a DNS tool for turbulent flows have been explored by a series of studies in homogeneous isotropic turbulence and turbulent channel flows [2–8]. However, DNS of turbulent flow in a circular pipe using LBM has not yet been reported, to our best knowledge. So far all successful DNS studies of turbulent pipe flow have been performed using conventional numerical methods based on directly solving the N–S equations. Eggels et al. [9] presented the first DNS of a fully developed turbulent pipe flow using a second-order finite-volume (FV) method based on a uniform grid in cylindrical coordinates. The bulk Reynolds number based on the domain-averaged mean flow speed U_b and the pipe diameter D of their DNS is $Re_b = U_b D / \nu = 5300$, which corresponds to a Reynolds number based on the friction velocity u_* and pipe radius R of $Re_\tau = u_* R / \nu = 180$. Here ν is the fluid kinematic viscosity. The turbulent statistics from their simulation were reported to be in reasonable agreements with those from Laser Doppler Anemometry (LDA) and Particle Image Velocimetry (PIV) measurements at $Re_b = 5450$. They confirmed that the logarithmic layer deviates from the classical log-law at this low flow Reynolds number due to the pipe curvature effect. Loulou et al. [10] performed DNS of a fully developed turbulent pipe flow at $Re_b = 5600$ using a B-spline pseudo-spectral method. Compared with the previous FV simulations, Loulou et al.'s pseudo-spectral method is much more accurate providing likely a true benchmark for turbulent statistics, although later in this paper we will find that even the spectral results are not always accurate due to inadequate pipe length and limited time duration of the simulation. Wagner et al. [11] investigated the effect of Reynolds number on the turbulent statistics of fully developed turbulent pipe flow by considering a range of flow Reynolds number from $Re_b = 5,300$ to 10,300, using a second-order FV method based on a non-uniform grid in the radial direction. The comparisons of turbulent statistics under different Re_b suggest the strong influence of flow Reynolds number on both mean and fluctuation flow properties. Wu and Moin [12] conducted a DNS study of turbulent pipe flows with Re_b up to 44,000 with a second-order FV method. More recently, Chin et al. [13] conducted a series of turbulent pipe flow DNS with a spectral method at $Re_\tau = 170$ and 500 for different pipe lengths. Their findings suggest the necessary pipe lengths to eliminate the pipe length dependence of the turbulent statistics are different in the inner and outer regions of a turbulent pipe flow. For the inner region (near the wall), the necessary pipe length is found to be at least 6300 times of the wall unit $y_* = \nu / u_*$, while for the outer region, the turbulent statistics become independent of the pipe length beyond approximately $4\pi D$. El Khoury et al. [14], performed a series of DNS in a turbulent pipe flow with different Reynolds numbers, $Re_\tau = 180, 360, 550$ and 1000. Based on their results, a comparison study was also carried out among turbulent flow statistics in a channel, pipe and boundary layer. Their work indicates that the pressure exhibits the most significant difference among the three wall-bounded turbulent flows.

Since turbulent pipe flow represents a more realistic flow often encountered in engineering applications, it is highly desirable to perform DNS of this flow with LBM in order to establish LBM as a viable alternative for turbulent flow simulation. For LBM simulations, the presence of a curved pipe wall adds a great deal of fundamental difficulties. The accurate representation of the curved pipe surface is essential since the majority of turbulent kinetic energy production and viscous dissipation is confined to the near-wall region. Unlike conventional CFD methods, such as the finite volume (FV) scheme, that can be applied to a computational mesh in cylindrical coordinates which allows accurate representation of the pipe wall [9–12], standard LBM is restricted to a cubic grid in Cartesian coordinates that does not conform with the cylindrical surface. Thus to resolve the pipe boundary in LBM, local interpolation is used which could introduce both inaccuracy and numerical instability. Although the boundary treatments on a curved boundary have received a great deal of attention in LBM [15–17], their impacts on the accuracy and numerical instability in a turbulent pipe flow simulation has not been systematically studied.

Previously, only large-eddy simulations (LES) of turbulent pipe flows have been attempted using LBM [6,18]. Those LES studies confirmed the existence of so-called lattice effects in the simulation of turbulent flow in a circular pipe due to the lack of isotropy in a D3Q19 lattice [19]. The "isotropy" means how well the discrete velocity set in LBM reproduces the physical isotropy as required by the N–S equations, such as the rotational invariance, meaning the simulation results should be independent of how the mesh grid is oriented. Kang and Hassan [6] conducted LES of turbulent pipe flow on both D3Q19 and D3Q27 lattice grids. Their results indicate that with the same simulation conditions, the mean and fluctuation velocities with D3Q27 are in reasonable agreement with the results of the DNS by Eggels et al. [9], while those with D3Q19 exhibited large deviations (up to 28% relative error) from the same DNS benchmarks [6]. Suga et al. [18] later presented a similar LES of turbulent pipe flow based on their proposed multi-relaxation time (MRT) LBM model with D3Q27 lattice grid. Their mean flow velocity and root-mean-squared (r.m.s.) velocity profiles are also in reasonable agreement with the corresponding DNS benchmarks in Eggels et al. [9]. These observations lead to the conclusion that D3Q19 is not suitable for the turbulent pipe flow simulation with LBM thus D3Q27 is the only option. Kuwata and Suga [20] employed a Taylor-expansion based analysis, and derived the analytical forms of truncation errors based on D3Q15, D3Q19 and D3Q27 lattice grid, in terms of N–S equations in cylindrical coordinate. They discovered that the error terms of radial and azimuthal velocity based on D3Q15 and D3Q19 grid depend on the radial derivatives of mean flow velocity while these error terms based on the D3Q27 lattice do not. This analysis offered a theoretical explanation on the lack of isotropy in a D3Q19 lattice. However, it is still questionable if this deficiency would lead to a significant inaccuracy in the turbulent statistics. As will become clear later, the capabilities and accuracy of a lattice model depend largely on the implementation details used to meet the no-slip boundary condition at the fluid–solid interface, as well as the grid resolution. In this paper, we will introduce a

novel implementation of LBM, to demonstrate that accurate statistics of a turbulent pipe flow is actually achievable even on a D3Q19 lattice, given a sufficient grid resolution.

We should note that there are some limited efforts to introduce cylindrical coordinates into LBM. One typical approach is the development of LBM models for axisymmetric flows [21–23]. The idea is to add a source term in the lattice Boltzmann equation (LBE) to reproduce the N–S equations in the cylindrical coordinates, when the flow has no azimuthal dependence. Although such methods allow one to simulate three dimensional axisymmetric flow on a two-dimensional lattice grid, which greatly enhances the computational efficiency, they cannot be used for the turbulent pipe flow simulations that depend on the azimuthal coordinate. Other approaches that could be relevant to DNS of a turbulent pipe flow are the finite-difference (FD) [24,25], FV [26–29] or spectral implementations [30] of the discrete-velocity Boltzmann equation, by uncoupling the discretization of physical space and lattice time. Those alternative Boltzmann-equation based approaches do allow the use of non-uniform grid in curvilinear coordinates to fit, for example, the circular pipe wall. However, compared with the standard LBM that uses direct streaming, these methods introduce additional diffusion and dissipation in the discretization of space and time, which may affect the accuracy of the simulated turbulent statistics. Moreover, they are less efficient in terms of parallel scalability when compared to the standard LBM.

The present work has three major objectives. First, we will develop a novel LBM implementation on a D3Q19 lattice and use it as a DNS tool for turbulent pipe flows. In order to achieve this goal, we have introduced improved methods both within the LBM scheme itself and at the fluid–solid interface to address issues related to accuracy and numerical instability in the presence of a curved wall. While the study here is limited to the turbulent pipe flow, the methods should have broader implications for simulating turbulent flows in complex geometries.

Second, in parallel to the D3Q19 simulation, we will perform a similar simulation based on the D3Q27 lattice with comparable parameter settings. The comparison of the implementation details and numerical results between the two simulations will serve as a comprehensive assessment of each scheme in the turbulent flow simulations with curved boundaries.

At last, we will conduct a careful comparison of the resulting turbulent statistics among our LBM and other conventional methods [9,11,10] as well as those from experimental measurements. Experimental data of turbulent pipe flows at moderate flow Re numbers include measurements using LDA [31][1] and PIV [32]. Such systematic comparisons will not only provide a fair assessment on the performance of our LBM, especially its boundary treatment schemes on the simulation of flow in a cylindrical geometry; but also reveal inaccuracies in some previous DNS and experimental data which should benefit the community in the future.

The rest of the paper is arranged as follows. In Sec. 2, we discuss the physical problem and the numerical method with all the implementation details for both D3Q19 and D3Q27 lattices. Due to numerical instability with the D3Q19 lattice grid, several efforts, including a MRT model with extended equilibria to enable moderate relaxation parameters, and a moving frame of reference to reduce the flow Mach number are introduced. A new bounce-back scheme is also applied to remove the violation of Galilean-invariance errors when the flow is fit in a moving frame of reference. On the other hand, the D3Q27 lattice grid is found to be numerically stable under the current setting, so the above treatments are not necessary. In Sec. 3, we first validate the method in a transient laminar pipe flow and briefly discuss the accuracy of the LBM models with both lattice grids. Then, in Sec. 4, the turbulent flow statistics are discussed systematically through a careful comparison with existing numerical and experimental results. A large number of flow statistics in both physical space and spectral space are analyzed. Finally, Sec. 5 contains a summary and the main conclusions of the present work. The Appendix gives all the details of the D3Q19 and D3Q27 MRT models used in the simulations. It also explains how the local vorticity is computed, and the necessary additional considerations to convert data from a Cartesian grid to flow field in cylindrical coordinates.

## 2. Problem statement and the simulation method

We consider the classical flow inside a circular pipe driven by a constant external force. As sketched in Fig. 1(a), r, θ and z represent the radial, azimuthal and streamwise directions, respectively. The radius of the pipe is R, the length of the pipe is L. Periodic boundary condition is assumed in the streamwise direction, while on the pipe wall, the no-slip boundary condition is applied.

A constant body force ρg (per unit volume), or equivalently a mean pressure gradient is applied in the streamwise direction to drive the flow. At the fully developed stage and averaged over time, force balance between the driving and the viscous force is established as $2\pi R L \langle \tau_w \rangle = \pi R^2 L \rho g$, which leads to the expression of the averaged wall shear stress $\langle \tau_w \rangle$ and the friction velocity u^* as

$$\langle \tau_w \rangle = \frac{1}{2}\rho g R, \quad u^* = \sqrt{\frac{\langle \tau_w \rangle}{\rho}} = \sqrt{\frac{gR}{2}}, \tag{1}$$

where ρ is the fluid density. The frictional Reynolds number can then be defined as $Re_\tau = u^* R / \nu = R/(\nu/u^*)$, where ν is the kinematic viscosity, $y^* = \nu/u^*$ is characteristic length scale of the viscous sublayer, which is known as the wall unit. The large-scale eddy-turnover time is defined as R/u^*.

---

[1] The data used for comparison is extracted from Ref. [32] since the original reference is in Dutch.
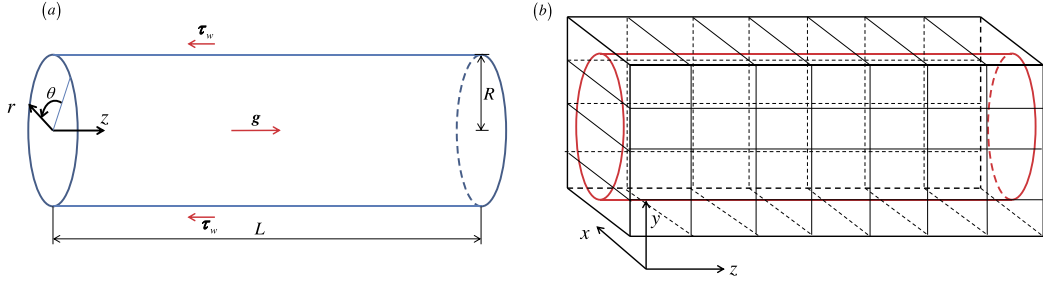
Fig. 1. Sketches of (*a*) the physical coordinate system used for the pipe flow and (*b*) the 2D domain decomposition for MPI implementation.

In this study, we set $Re_\tau = 180$, in order to benchmark our results with the database from the other published DNS studies based on the pseudo-spectral (PS) and FV methods. The bulk Re number, defined with the mean flow velocity magnitude $\bar{U}$ and pipe diameter D, is around 5300. The velocity scale ratio is $\bar{U}/u^* \approx 14.7$.

2.1. The lattice Boltzmann method

Unlike conventional or macroscopic CFD methods that solve the incompressible Navier–Stokes equations, LBM amounts to solving the weakly compressible N–S equations with a model speed of sound c_s ($c_s = 1/\sqrt{3}$ in the lattice units for both D3Q19 and D3Q27 lattice grids). Such feature confines the maximum flow speed in order to ensure that the maximum local Mach number is small. Under this constraint, to achieve a high Re with a manageable mesh size, the viscosity ν in the simulation usually needs to be very small. In LBM, the fluid viscosities are related to the relaxation parameters, small viscosities may lead to a severe numerical instability.

Based on this consideration, the MRT LBM model is adopted due to its enhanced numerical stability. Compared with the Lattice Bhatnagar–Gross–Krook (LBGK) collision operator that relaxes all the molecular distribution functions with a single relaxation parameter, MRT collision operator is constructed in the moment space, to allow different moments to relax with different relaxation parameters. The relaxation parameters associated with moments irrelevant to the N–S equations can be optimized for better numerical stability [33,34]. For example, in a MRT model, one is allowed to choose different relaxation parameters for the energy and stress moments, which leads to an adjustable bulk viscosity in the resulting hydrodynamic equations. The bulk viscosity is irrelevant for the incompressible N–S equations, but larger values of bulk viscosity were found to enhance the numerical stability of LBM by damping out the acoustic noises more quickly [35,36]. In LBGK models, the ability of tuning the bulk viscosity is not available. The evolution equation of the MRT LBM reads as

$$\mathbf{f}(\mathbf{x} + \mathbf{e}_i \delta_t, t + \delta_t) - \mathbf{f}(\mathbf{x}, t) = -\mathbf{M}^{-1}\mathbf{S}\left[\mathbf{m}(\mathbf{x}, t) - \mathbf{m}^{(eq)}(\mathbf{x}, t)\right] + \mathbf{M}^{-1}\mathbf{\Psi}, \tag{2}$$

where $\mathbf{f}$ is the distribution function vector, t and $\mathbf{x}$ are the time and spatial coordinate, respectively. $\mathbf{e}_i$ is the lattice particle velocity in the i direction. δ_t is the time step size. $\mathbf{M}$ is the transformation matrix, which transforms the distribution function vector $\mathbf{f}$ into a moment vector $\mathbf{m}$ as $\mathbf{m} = \mathbf{Mf}$ and $\mathbf{f} = \mathbf{M}^{-1}\mathbf{m}$, $\mathbf{M}^{-1}$ is the inverse matrix of $\mathbf{M}$. $\mathbf{m}^{(eq)}$ is the equilibrium part of $\mathbf{m}$. $\mathbf{S}$ is a diagonal matrix containing all the relaxation parameters. $\mathbf{\Psi}$ represents the mesoscopic external force vector. The detailed descriptions of these terms are given in the Appendix for the D3Q19 and D3Q27 lattices.

2.2. Parameter set-up

The grid resolution in a direct numerical simulation must be able to resolve the smallest length scale in a flow, *i.e.*, Kolmogorov length scale $\eta = (\nu/\epsilon)^{(1/4)}$, ϵ is the local dissipation rate. Based on the published DNS dataset from spectral simulations [37,10], for $Re_\tau = 180$, the local dissipation rate on the wall has a value of $\epsilon^+ \approx 0.16$ (hereafter we use the superscript + to denote quantities normalized by the wall unit y^* or friction velocity u^*). Using this data, the local Kolmogorov length scale for the near-wall region is about $\eta^+ = 1.5$. In wall-bounded turbulence, the local Kolmogorov length scale increases as the location moves away from the wall, thus $\eta^+ = 1.5$ can be viewed as the smallest length scale in our turbulent pipe flow. Lammers et al. [3] suggested that for LBM, a sufficient grid resolution in a turbulent channel flow DNS with $Re_\tau = 180$ should be $\delta_x^+ \leq 1.5$. Due to the similarity between a turbulent channel flow and a turbulent pipe flow under such a low Reynolds number, this criterion should also apply in our turbulent pipe flow simulation. Alternatively, previous DNS studies of wall-bounded turbulent flows [38,9] suggested a sufficient grid resolution usually required three grid points inside the viscous sublayer ($(R - r)/y^* \leq 8$), which translate to a criterion of $\delta_x^+ \leq 2.5$ for a uniform grid. With the above considerations, we choose $R = 148.5$ in lattice units, which implies that $\delta r^+ = 180/148.5 \approx 1.212$. This grid spacing is sufficiently small to resolve all scales even for the near wall region. On the other hand, the pipe length in the streamwise direction must be long enough to minimize the effect of the periodic boundary condition [13]. In the present work, we set $L = 1799$, which is roughly $12.11R$. Although this pipe length does not meet the suggested pipe length in [13] to obtain fully pipe-length-independent turbulent statistics near the pipe wall, it allows fair comparisons among the results

Table 1
Physical parameters used for the simulation of turbulent pipe flow. All the parameters are given in lattice unit, i.e., $\delta_x = 1$, $\delta_y = 1$.

Case	$N_x \times N_y \times N_z$	ν	ν^V	R	u^*	Re_τ	$\delta x/y^*$
D3Q19	$300 \times 300 \times 1799$	0.0032	1.0	148.5	0.00388	180	1.212
D3Q27	$300 \times 300 \times 1799$	0.0032	0.0032	148.5	0.00388	180	1.212

Table 2
LBM model parameters used in the LBM simulations (top: D3Q19 extended MRT model; bottom: D3Q27 MRT model).

α_{16}	β_{16}	γ_{17-18}	s_{1-3}	s_4	s_{5-9}	s_{10-12}	s_{13-15}	s_{16}	s_{17-18}	ζ	λ
0	$-475/63$	0	1.0	1.0	1.8	1.8	1.5	1.5	1.5	-0.889	0.0153

α_{17}	β_{17}	β_{18-19}	γ_{20-22}	ζ_{23-25}	α_{26}	β_{26}	s_{1-26}
2.0	-4.0	-1.0	-1.0	1.0	-1.0	3.0	$\frac{1}{(3\nu+0.5)}$

of our present simulation and those existing datasets, which were obtained with a pipe length of about 10R [9,11,10]. While the physical problem is stated in a cylindrical coordinate, i.e., r, θ, z coordinates, the LBM simulation is set up in the Cartesian coordinates, i.e., x, y and z. Based on the two aforementioned aspects, the grid resolution is chosen to be $N_x \times N_y \times N_z = 300 \times 300 \times 1799$. The whole computation domain is decomposed in the x and z directions as 90×15 subdomains using 2D domain decomposition as shown in Fig. 1(b). The data communication between neighboring domains is handled with Message Passing Interface (MPI). More details about the code parallelization and scalability can be found in a recent paper by Geneva et al. [39]. Although larger numbers of variables are solved at a given node when compared to the conventional N–S solvers, compensated by its excellent scalability in parallel computing, LBM still acts as a competitive tool for CFD, especially when complex geometries are involved. Under the current setting, each time step in the D3Q19 simulation and D3Q27 simulation takes roughly 0.057 seconds and 0.076 seconds, respectively, when 1,350 cores are used. Each simulation takes about 30 eddy turnover times to develop into statistical stationary state and 50 eddy turnover times to gather data for time averaging, which translates to 3,000,000 in time steps, and costs 48.5 and 64.6 hours in physical time for the D3Q19 and D3Q27 simulations, respectively.

The pipe center of the D3Q27 simulation is placed in the x–y plane at $r_c = (150, 150)$, which collapses with the geometric center of the computational domain. The pipe center of the D3Q19 simulation, on the other hand, is slightly shifted to $r_c = (150.5, 150.5)$. The shifting of the physical pipe center relative to computational domain center creates artificial asymmetry in the boundary-link configuration, which is designed to reduce the symmetric spurious secondary-flow patterns observed in [19], [6] and [18]. The kinematic viscosity ν is chosen to be 0.0032 in both D3Q19 and D3Q27 simulations. The bulk viscosity ν^V in the D3Q19 simulation is set to 1.0 in order to more quickly damp out the acoustic waves in the flow [36], while ν^V in the D3Q27 simulation is made identical to the shear viscosity ν. The difference here, as we shall see shortly, is mainly because the D3Q19 simulation needs to be performed in the moving frame of reference to maintain numerical stability, where the moving walls in LBM usually result in more severe acoustic waves. The D3Q27 simulation, on the other hand, is found to be numerically stable under the same physical conditions of the D3Q19 simulation. For D3Q27, the moving frame of reference is not necessary, thus there is no need to use a large bulk viscosity. The use of a large bulk viscosity may contaminate the pressure field, which must be corrected, as explained in Section 4.3. The key parameters used in the present study are summarized in Table 1 and Table 2. Specifically, in the D3Q19 extended MRT model, ζ and λ are defined according to Eq. (21) so the relaxation parameters s_4 and s_{5-9} can be set to 1.0 and 1.8, respectively, for the optimized numerical stability. In the D3Q27 simulation, all the relaxation parameters are set to be the same. This is already enough to ensure numerical stability in the current simulation so no further optimization of the relaxation parameters is made.

2.3. Flow initialization and prescribed excitation at the early stage

The flow is initialized with the following mean velocity profile containing the viscous sublayer profile and inertial sublayer (or logarithmic) profile

$$U^+\left(\delta^+\right) = \begin{cases} \delta^+, & \text{if } \delta^+ \leq 10.8, \\ \frac{1}{0.4} \ln\left(\delta^+\right) + 5.0, & \text{if } \delta^+ > 10.8, \end{cases} \tag{3}$$

where $\delta = R - r$ is the distance from the pipe wall. It should be noted that, although in a fully developed turbulent pipe flow, the mean velocity profile does not strictly conform with Eq. (3) in the logarithmic region [9,40,10], the developed flow mean velocity profile should not be affected by this initial condition. While this initial velocity field is not a solution of the N–S equations, it is expected to stretch the vortices in the flow more quickly, compared to starting the flow from rest, which may serve the purpose of speeding up the flow transition to a realistic, fully developed turbulent pipe flow. The initial distribution functions are simply set to the equilibrium distributions in the D3Q27 simulation, i.e., $\mathbf{f} = \mathbf{M}^{-1}\mathbf{m}^{(eq)}$, and

the leading-order equilibrium distributions in D3Q19 simulation, *i.e.*, $\mathbf{f} = \mathbf{M}^{-1}\mathbf{m}^{(eq,0)}$, based on the initial velocity field and zero initial pressure.

The flow is forced by the body force $(F_r, F_\theta, F_z) = (0, 0, \rho_0 g)$. To accelerate the transition from the initial laminar flow to turbulence, we add a non-uniform, divergence-free force field to the flow only during the first three large-eddy turnover times of the simulation, namely,

$$F'_r = -g\kappa B_0 \frac{R}{r}\frac{k_z l}{L}\sin\left(\frac{2\pi t}{T}\right)\left\{1 - \cos\left[\frac{2\pi (R - r - l_0)}{l}\right]\right\}\cos\left(k_z\frac{2\pi z}{L}\right)\cos(k_\theta\theta) \tag{4a}$$

$$F'_\theta = g(1 - \kappa) B_0 \frac{k_z}{k_\theta}\frac{2\pi R}{L}\sin\left(\frac{2\pi t}{T}\right)\sin\left[\frac{2\pi (R - r - l_0)}{l}\right]\cos\left(k_z\frac{2\pi z}{L}\right)\sin(k_\theta\theta) \tag{4b}$$

$$F'_z = -g B_0 \frac{R}{r}\sin\left(\frac{2\pi t}{T}\right)\sin\left[\frac{2\pi (R - r - l_0)}{l}\right]\sin\left(k_z\frac{2\pi z}{L}\right)\cos(k_\theta\theta) \tag{4c}$$

where k_z and k_θ are the wavenumbers of the perturbation force in streamwise and azimuthal directions, respectively. T is the forcing period, B_0 is the forcing magnitude, κ is the weighting parameter that distributes the perturbation in radial and azimuthal directions. The above forcing is added only to the region $l_0 \leq R - r \leq l_0 + l$ in radial direction. After the initial period of three eddy turnover times, the perturbation forcing is no longer applied, namely, $(F'_r, F'_\theta, F'_z) = (0, 0, 0)$ for $t \geq 3R/u^*$. The purpose of this perturbation force is to create large-scale vortex structures in the initial flow field. These vortices are stretched by the mean flow and break into small vortices, promoting energy cascade in turbulence. A very similar perturbation force field was designed and tested in our previous turbulent channel flow simulations [8]. Similar ideas of triggering turbulence were also proposed in [41,42], but in the Fourier space.

In this paper, since we focus only on the fully developed stage of the turbulent pipe flow, how to drive the flow to its stationary turbulence can be flexible. To save computational resources, the simulation is started in a smaller domain with $N_{0x} \times N_{0y} \times N_{0z} = 300 \times 300 \times 599$, which reaches a turbulent flow field after about 30 eddy turnover times. For the starting smaller domain, the parameters in Eq. (4) are chosen as: $k_z = 3$, $k_\theta = 2$, $T = 2000$, $l_0 = 0.2R$, $l = 0.4R$, $B_0 = 50.0$, $\kappa = 0.5$. At this stage, the flow is already fully developed, but for a 1/3 pipe length. We then copied this flow twice to form a new starting flow field. Since the streamwise domain size 1799 is not an exact multiple of 599, the missing information for two gap layers (with grid indices $n_z = 600$ and $n_z = 1200$) between copies is filled by a simple linear extrapolation scheme, as

$$f_i(n_x, n_y, 600) = 2f_i(n_x, n_y, 599) - f_i(n_x, n_y, 598), \tag{5a}$$

$$f_i(n_x, n_y, 1200) = 2f_i(n_x, n_y, 1199) - f_i(n_x, n_y, 1198). \tag{5b}$$

Once the copy and extension are done, the flow takes about another 10 eddy turnover times to depart the imposed periodicity and reach the stationary stage in the full domain.

2.4. The use of a moving frame and improved implementation at the pipe wall

The interpolated bounce-back rule is applied on the pipe wall to maintain the overall second-order accuracy in the simulation. While both linear and quadratic interpolation schemes possess at least the second-order spatial accuracy, they have significant difference in terms of numerical stability in the present simulation. Although the quadratic interpolation schemes have generally better accuracy than the corresponding linear interpolation schemes [43], they are not numerically stable in the present turbulent pipe flow simulation, for both D3Q19 and D3Q27 lattices. The reason could be related to the appearance of negative coefficients in front of the distribution functions on the furthest node point in the quadratic interpolation schemes [15,17]. Furthermore, due to their lower accuracy in the interpolation, linear schemes tend to introduce larger numerical dissipation to the near wall region than quadratic schemes. Although this numerical dissipation negatively affects physical accuracy, it may enhance the numerical stability locally. For these reasons, in the present simulation, the linear interpolated bounce-back schemes by [15] and [17] are applied, and both of them are found to be numerically stable.

The checkerboard instability is another major problem encountered in the D3Q19 simulation. This instability problem is not observed in the D3Q27 simulation. Unlike the instability results from the quadratic interpolation schemes that originates from the pipe wall, the checkerboard instability appears first in the pipe center region and quickly propagates to the whole flow field, as shown in Fig. 2. The checkerboard instability is mainly due to the insufficient discretization of the mesoscopic velocity space that causes the distribution functions at one node point to isolate from its surrounding neighbors [44]. Because the D3Q27 lattice uses 8 more discrete velocities to discretize the mesoscopic velocity space than the D3Q19 lattice, its simulation is free of the checkerboard instability under the same physical parameter setting. Normally, such checkerboard instability can be eliminated by applying odd numbers of grid points in periodic directions, as indicated in [44] and [8]. However, this simple solution does not apply to the current pipe flow simulation. We tested both 599 and 600 lattice points in the streamwise direction in our D3Q19 simulation, but the same checkerboard pattern was observed. In this simulation, the checkerboard instability is found to be strongly related to the Mach number (Ma) in the center region of the pipe, which puts a much more critical confinement on the maximum allowed Ma in the pipe flow simulation than in the our previous channel flow simulations with the same Re_τ [8].
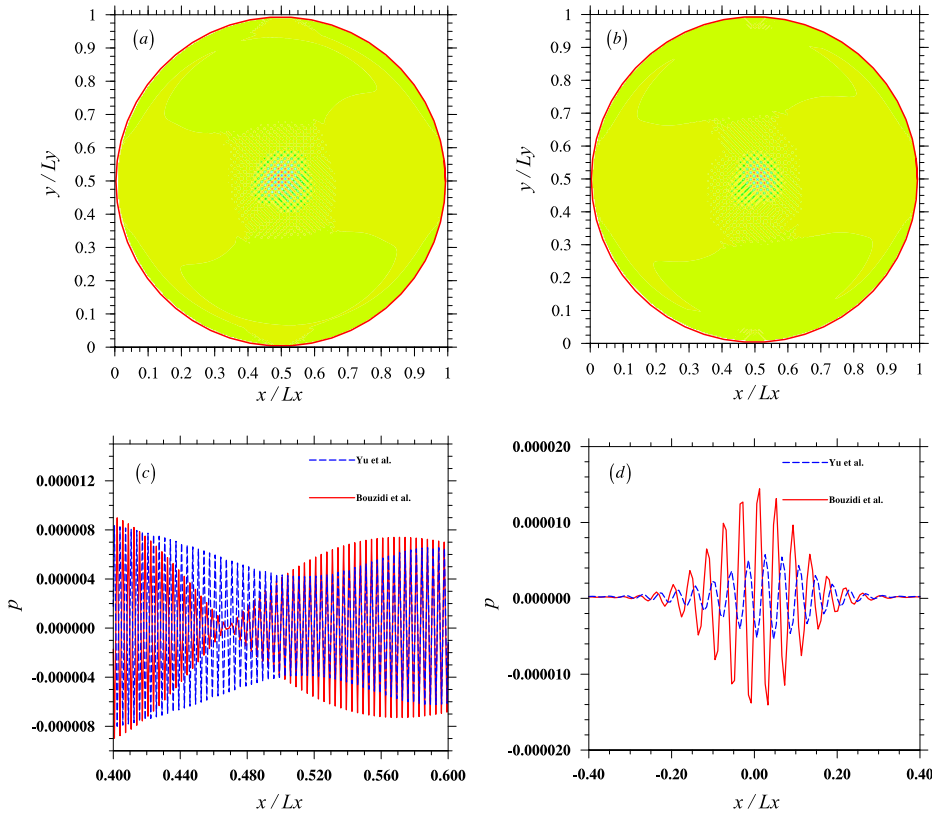
Fig. 2. The pressure pattern caused by the checkerboard instability. (*a*) Pressure contour in a cross section with Bouzidi et al.'s linear interpolated bounce back, (*b*) same as (*a*) with Yu et al.'s linear interpolated bounce back, (*c*) pressure distribution on a line along the streamwise direction, (*d*) pressure distribution on a line along the radial direction. The grid resolution is $N_x \times N_y \times N_z = 300 \times 300 \times 599$.

To reduce the local *Ma* number in the pipe center region, a negative (opposite to the driving force or mean flow) reference velocity is added to the whole system in the D3Q19 simulation, namely, we force the pipe wall to move at $u_w = -12u^*$. In N–S equations based CFD methods, the moving frame of reference was sometimes used to reduce the Courant–Friedrichs–Lewy (CFL) number constraints [45]. Physically, this constant translation velocity of the moving reference frame shall have no effect on the simulation results. Unfortunately, we discovered that the principle of Galilean invariance can be violated by the use of interpolated bounce-back schemes [46], *i.e.*, the shear stress provided by the pipe wall varies with the reference velocity that creates a significant violation of Galilean invariance (VGI) error in the mean flow velocity (see Sec. 4 for more details).

To solve this problem, we developed a new bounce-back scheme using the idea of coordinate transformation. The essential idea is to always perform the bounce-back operation in the frame moving with the wall. That is, the distribution functions involved in the interpolated bounce-back are transformed from the coordinate system attached to the lattice grid to a coordinate system moves with the pipe wall before the bounce-back, and transformed backward after the bounce-back. For further details, the readers are referred to [46] where several validation cases are presented for this new implementation based on the coordinate transformation. This transformation method can be incorporated with any interpolation scheme. In the present study, the linear interpolation scheme of Yu et al. [17] is specifically chosen.

It should be noted that the moving frame of reference as well as the new bounce-back schemes are only used in the D3Q19 simulation. The D3Q27 simulation is found free from the checkerboard instability under the current parameter setting, so the moving frame of reference is not necessary. In this sense, the D3Q27 lattice is of better numerical stability than the D3Q19 lattice. However, the moving frame of reference and new bounce-back condition can also be used for the D3Q27 lattice when the simulation conditions change.

3. Validation against the transient laminar pipe flow and accuracy analysis

Before discussing the LBM simulations of the turbulent pipe flow, we first validate our models and boundary treatments in a transient laminar pipe flow using both D3Q19 and D3Q27 lattice grids. Specifically, the extended D3Q19 MRT model and the bounce-back scheme for the moving frame of reference are relatively new, so the second-order accuracy in the code must be calibrated. In this case, we fix the Reynolds number $Re = (u_c - u_w)D/\nu$ at 100, where u_c is the flow velocity at the
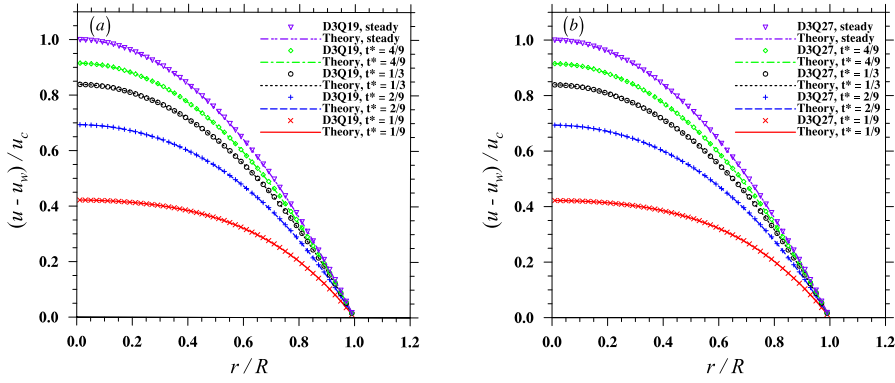
Fig. 3. Velocity profiles at six different times in a transient laminar pipe flow simulation: (a) D3Q19 extended MRT with $u_w = -u_c$, (b) D3Q27 MRT with $u_w = 0$.

Table 3
The L2 norm and convergence rate of the numerical error of the present implementation in a laminar pipe flow simulation (top: D3Q19 extended MRT with $u_w = -u_c$, bottom: D3Q27 MRT with $u_w = 0$). The convergence order is calculated as $\log_2[\epsilon_{L2}(D_1)/\epsilon_{L2}(D_2)]$, where D_1 and D_2 are two successive pipe radii, $D_1 < D_2$.

D/δ_x	$\varepsilon_{L2}(t^* = 1/3)$	Order	$\varepsilon_{L2}(t^* = 1.0)$	Order	$\varepsilon_{L2}(t^* = \infty)$	Order
45	6.227E−4	(−)	7.793E−4	(−)	7.837E−4	(−)
90	8.474E−5	2.877	1.150E−4	2.761	1.157E−4	2.760
180	1.855E−5	2.192	2.388E−5	2.268	2.405E−5	2.266
Overall		2.534		2.514		2.513
D/δ_x	$\varepsilon_{L2}(t^* = 1/3)$	Order	$\varepsilon_{L2}(t^* = 1.0)$	Order	$\varepsilon_{L2}(t^* = \infty)$	Order
45	3.341E−4	(−)	4.327E−4	(−)	4.386E−4	(−)
90	4.203E−5	2.991	4.759E−5	3.185	4.818E−5	3.186
180	1.055E−5	1.994	1.499E−5	1.667	1.530E−5	1.655
Overall		2.492		2.426		2.421

centerline when flow reaches the steady state, and u_w is the pipe wall velocity. Three pipe diameters in lattice units, $D = 45$, $D = 90$ and $D = 180$ are tested in order to reveal the order of accuracy of our implementation. For each pipe diameter, in the D3Q19 simulations, we fix the shear and bulk viscosity at 0.025 and 1.0, respectively, while in the D3Q27 simulations, the two viscosities are both chosen at 0.025. The parameters of each MRT model are chosen identically to those listed in Table 2, except that λ is adjusted to -0.00648 due to a different shear viscosity compared to that in the turbulent pipe flow, as indicated by Eq. (21b). The pipe wall velocity in the D3Q19 simulation is set to $u_w = -u_c$ to examine the moving frame of reference, while in the D3Q27 simulation, the pipe wall is static. The flow starts from a uniform field of velocity u_w and is driven by a uniform body force given as $16\nu(u_c - u_w)/D^2$. With $D = 90$, the velocity profiles at different non-dimensional times (normalized by $D^2/(4\nu)$) for both the D3Q19 and D3Q27 simulations are compared with the theoretical solutions in Fig. 3. The LBM results of the flow velocity on the Cartesian nodes are binned with 50 equally-spaced bins based on the position relative to the pipe center. As clearly indicated in Fig. 3, our implementations accurately predict the flow velocity for both the D3Q19 and D3Q27 cases. The L2 norms of the numerical errors for different pipe diameters at several dimensionless times are calculated and presented in Table 3. The L2 norm is defined as

$$\varepsilon_{L2} = \frac{\sqrt{\sum_\mathbf{x} |u_n(\mathbf{x}) - u_t(\mathbf{x})|^2}}{\sqrt{\sum_\mathbf{x} |u_c(\mathbf{x})|^2}}, \tag{6}$$

where u_n and u_t are the streamwise velocities from LBM and the analytical solution, respectively. The summation in the above equations are over all node points within the pipe radius. For both the D3Q19 and D3Q27 cases, Table 3 shows that the overall accuracy of the present implementations are of second order. The results based on the L1 norm (not shown) yield the same conclusion.

4. Turbulent pipe flow

In this section, we compare systematically the results from our LBM simulations of turbulent pipe flow to previous results in the literature. In Table 4 we summarized the key parameters from different studies which are considered here for comparison. Although both the Reynolds number dependence and pipe length dependence are reported for the turbulent pipe flow, these dependences have a negligible impact, for the parameter ranges shown in Table 4.

Table 4

Physical and simulation parameters in the turbulent pipe flow. The equivalent resolution of our simulation near the pipe wall, in terms of cylindrical coordinates, is also indicated.

	Method	Re_τ	$N_r \times N_\theta \times N_z$	L_z/D	Resolution $(\Delta r^+, \Delta z^+, R\Delta\theta^+)$
Tahitu	LDA	181.2	–	–	–
Westerweel et al.	PIV	181.2	–	–	(11.4, 4.51, 11.4)
Eggels et al.	2nd order FV, uniform grid	180	$96 \times 128 \times 256$	5	(1.88, 7.03, 8.83)
Loulou et al.	b-spline PS	190	$72 \times 160 \times 192$	5	(0.39–5.7, 9.9, 7.5)
Wagner et al.	2nd order FV, non-uniform grid	180	$70 \times 240 \times 486$	5	(0.36–4.32, 3.7, 4.7)
Present	LBM	180	$N_r: 105 \to 149$ $N_\theta: 660 \to 933$ $N_z: 1799$	6.06	(1.21, 1.21, 1.21)
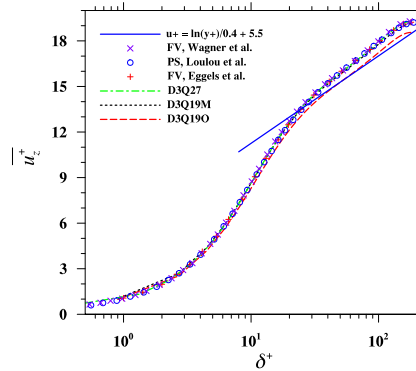
Fig. 4. The mean velocity profiles normalized by the wall units.

Only the fully-developed stage is considered in this paper. The results from the pseudo-spectral method by Loulou et al. [10] will be used as the benchmark due to the superior accuracy of the PS method. Our LBM results are first converted from Cartesian coordinate to cylindrical coordinate via volumetric binning. The detail of this process can be found in the Appendix.

4.1. Mean flow properties

We first examine the mean flow velocity profiles. In Fig. 4, the curves labeled "D3Q19O" and "D3Q19M" represent the profiles of D3Q19 simulation with Yu et al.'s original interpolated bounce-back scheme [17] and the modified scheme with coordinate transformation but based on the same interpolation strategy [46], respectively. Due to the VGI error associated with the moving boundary in the D3Q19 simulation, the former deviates from the other profiles significantly. On the contrary, the modified scheme effectively suppresses the VGI error leading to a profile that is in excellent agreement with those from the PS and FV methods. The curve labeled "D3Q27" is the profile from the D3Q27 simulation that uses static wall. This profile also matches well with the benchmark results. Unlike the previous LES results reported by Kang & Hassan [6], where the mean velocity profile of D3Q19 simulation deviates significantly from the benchmark results, in our simulations as far as the VGI error is suppressed, the D3Q19 and D3Q27 results are both accurate. A well-known fact of the mean velocity profiles at the low Reynolds numbers in a turbulent pipe is the deviation from the classical logarithmic law. Our simulation results also confirm such phenomenon.

For low-*Re* turbulent pipe flows, due to the insufficient separation of inner and outer scales, the mean velocity result can be normalized by either the inner scale (friction velocity, as in Fig. 4) or the outer scales (bulk flow velocity). The mean velocity profiles normalized by the bulk velocity (the respective domain-averaged flow speed and pipe radius) are shown in Fig. 5. Interestingly, under this scaling, the result of D3Q19O matches the other results well, indicating it has the same shape as other LBM profiles under the outer scaling. This result confirms that the un-modified interpolation bounce-back method overestimates the friction velocity, which is an outcome of the VGI error leading to an incorrect wall shear stress.

4.2. Basic turbulence statistics

The Reynolds stress profiles are compared in Fig. 6. The straight line indicates the total stress $-\overline{u_z'^+ u_r'^+} + dU_z^+/dr^+ = r/R$, which can be obtained from the momentum balance equation in the streamwise direction. As shown in Fig. 6, both D3Q19 results are in good agreement with the other DNS results, implying the VGI error does not have an obvious impact on the turbulent fluctuations. This makes sense because the turbulent stress measures the level of velocity fluctuation which is independent from the frame of reference. Again, no visible difference is observed among the Reynolds stress profiles
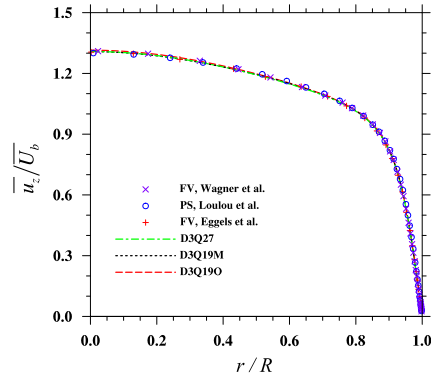
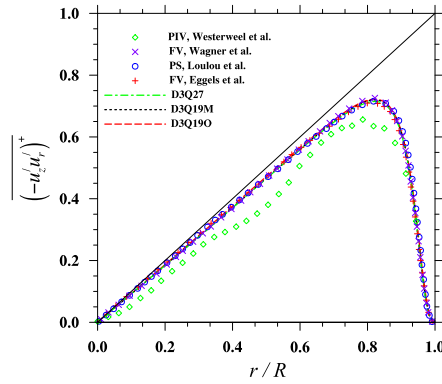**Fig. 5.** The mean velocity profiles normalized by the bulk flow velocity.

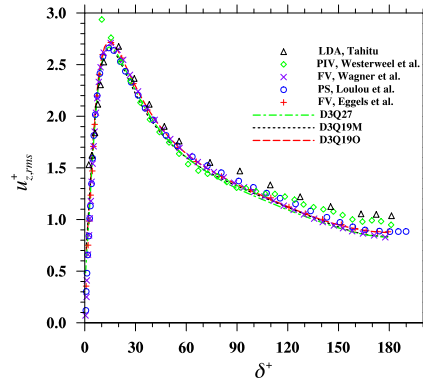**Fig. 6.** The Reynolds stress profiles as a function of radial location.

Fig. 7. Profiles of the r.m.s. velocity fluctuations in the streamwise direction.

from D3Q19 and D3Q27 simulations. The PIV measurement result, however, exhibits significant differences from the DNS counterparts, which is mainly because of the sampling error resulted from insufficient spatial resolution and sampling time in the experimental measurement [32].

Root mean squared (r.m.s.) fluctuation velocity profiles in the streamwise, radial, and azimuthal directions are shown in Fig. 7, Fig. 8, and Fig. 9, respectively. Very good overall agreements are obtained among the LBM results and the PS benchmark results. Again, the VGI error only introduces a minor effect on the r.m.s. velocity profiles. Slight visible differences between two D3Q19 profiles are observed only in the regions around the profile peaks and very close to the pipe center. The modified boundary treatment in the D3Q19 simulation always leads to slightly smaller velocity fluctuations compared to the original treatment, which yields a slightly better match with the PS results in the buffer region but slightly worse agreement near the pipe center. The r.m.s. velocity profiles of the D3Q27 simulation are also in slightly better agreements with the D3Q19 results with modified boundary treatment than those with original boundary treatment.
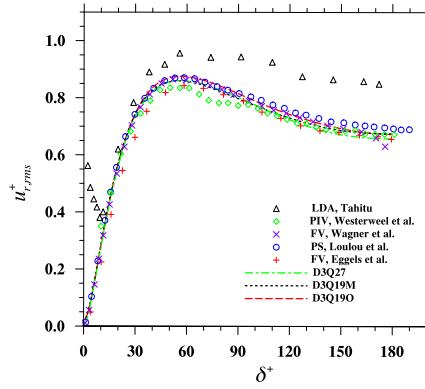
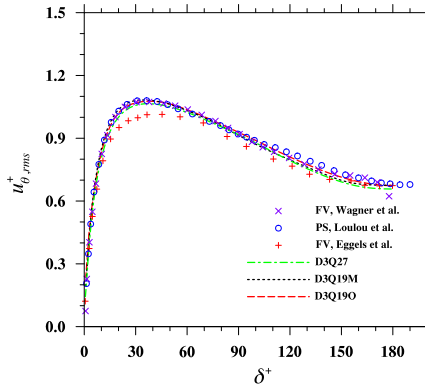**Fig. 8.** Profiles of the r.m.s. velocity fluctuations in the radial direction.

Fig. 9. Profiles of the r.m.s. velocity fluctuations in the azimuthal direction.

It is worth noting that the FV profiles of Eggels et al. [9] fail to follow the PS results around the local maximums in Fig. 8, and Fig. 9, with relative errors of about 5% and 10%, respectively. This could be mainly due to their use of a uniform grid in the radial direction causing the near wall region to be inadequately resolved (see Table 4). The grid resolution in our LBM simulations is $\delta r^+ = 1.212$, compared to $\delta r^+ = 1.88$ used in [9]. As we have analyzed in Sec. 2.2, the grid resolution for the near wall region needs to go below the Kolmogorov length scale on the wall ($\eta^+ = 1.5$). Our resolution is able to resolve this smallest scale in the flow while the resolution used by Eggels et al. [9] may not. Furthermore, since the advection term in LBM is treated exactly (except at the pipe wall where the interpolated bounce back is introduced), a much smaller numerical dissipation is usually expected in LBM that potentially leads to more accurate results when compared to the second-order FV method used by Eggels et al. [9].

It is interesting to note that while our LBM simulation based on D3Q19 lattice grid presents highly accurate mean and r.m.s. velocity results compared to PS results, significant (up to 30%) deviations were reported in previous LES study [6]. Such deviations were attributed to the lack of isotropy of D3Q19 in representing circular pipe boundary, since the results from the simulation based on D3Q27 lattice that has better isotropy showed good agreement with the FV results by Eggels et al. [9]. Based on our comparisons above, we suggest that the FV simulation on uniform grid by Eggels et al. [9] should not be used as the benchmark. Also, it is more likely that the large deviations reported in the previous LES study [6] are partially due to the insufficient resolution (the highest resolution in that study was $\delta r^+ = 3.6$) for the near wall turbulence. Due to the lack of grid resolution, the general good results based on the D3Q27 lattice grid in [6] are also questionable. Since the modified bounce-back scheme only brings a significant improvement on the mean flow velocity, for the sake of simplicity, from now on we no longer include the results with the original bounce-back scheme in the discussions. All the D3Q19 results discussed later are referred to the D3Q19M results.

According to the radial momentum balance equation, the mean pressure can be related to the r.m.s. velocities in the radial and azimuthal directions as

$$\frac{1}{\rho}\overline{P}(r) + \overline{u_r^2}(r) + \int_r^R \frac{\overline{u_\theta^2}(r) - \overline{u_r^2}(r)}{r}dr = \frac{1}{\rho}\overline{P}(R) = const. \tag{7}$$

This balance is well captured by our LBM results for most of the region as shown in Fig. 10, where $\langle P \rangle$, $\langle \Phi \rangle$ and $\langle \zeta \rangle$ correspond to the first, second and third terms on the LHS of Eq. (7), respectively. It is worth emphasizing that LBM solves
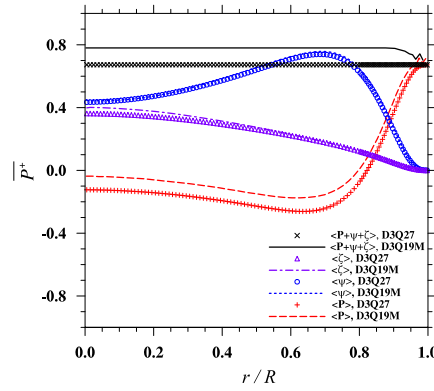
Fig. 10. The mean pressure profile and the balance against the transverse (radial and azimuthal) r.m.s. velocity fluctuations.
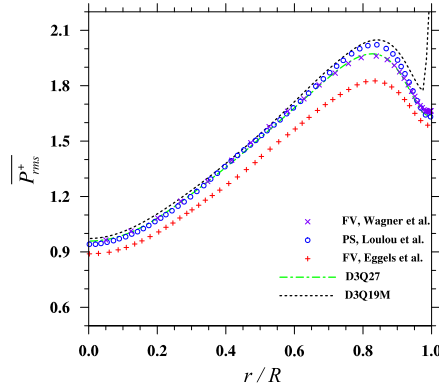

**Fig. 11.** Profiles of the r.m.s. pressure fluctuations.

the weakly compressible N–S equations with a divergence term that on the order of $O(Ma^2)$. Compared with the fully incompressible N–S equations, the *incompressible-equivalent* definition of the pressure from LBM should be

$$P = \tilde{P} + \rho \left[\frac{2}{3} \nu \left(\nabla \cdot \vec{u} \right) - \nu^V \left(\nabla \cdot \vec{u} \right) \right] \tag{8}$$

where $\tilde{P} = c_s^2 \delta \rho$, and P is the corrected pressure that resembles the incompressible flow. In our D3Q19 simulation, due to the use of the large bulk viscosity ($\nu^V = 1.0$ compared to $\nu = 0.0032$), the error caused by the third term on RHS of Eq. (8) is significant and must be removed using the above pressure correction in order to satisfy Eq. (7). Very close to the pipe wall, the D3Q19M pressure profile exhibits small fluctuations and a slight deviation of the constant sum in the region $r/R > 0.92$. This is likely results from the pressure noise associated with the moving boundary in LBM (as demonstrated later). In the post-processing, the integral term is computed by Simpson's rule. In the D3Q27 simulation, since the pipe wall is static, much less pressure noise is generated. Thus the balance in Eq. (7) is perfectly maintained over the whole pipe. The constant pressures on the pipe wall are slightly different in the D3Q19 and D3Q27 simulations. These values are determined by the boundary link configurations and the pipe wall velocities, which are both different in the D3Q19 and D3Q27 simulations.

The r.m.s. pressure profiles are presented in Fig. 11. In the D3Q19 result, the sudden jump near wall is mainly due to noises associated with the acoustic waves at the moving curved boundary, as indicated by an instantaneous snapshot of the pressure contour at a cross section (here $z = (N_z - 1)/2$) in Fig. 12(a). This sudden jump does not appear in the D3Q27 simulation, where the static pipe wall leads to much smaller pressure noise (Fig. 12(b)). Again, the r.m.s. pressure profiles of LBM are in better agreement with the PS profile than the FV results of Eggles et al. [9], which contains roughly 10% relative error when compared with the PS result of [10]. The D3Q27 profile matches specifically well with the FV results based on non-uniform grid of Wagner et al. [11]. It is well known that LBM only has a first-order accuracy for the pressure calculation. However, since the pressure in LBM is derived from precise moment calculation, it may still prevail over the second-order FV method, which solves the pressure Poisson equation to update the pressure field.

Next, the averaged dissipation rate profiles are presented in Fig. 13. The two LBM results collapse with each other and are in very good agreement with the other benchmark results, except the region near the pipe wall $\delta^+ < 5$. In this small region, the local dissipation rate of D3Q19 simulation is larger than that of D3Q27 simulation. This additional dissipation
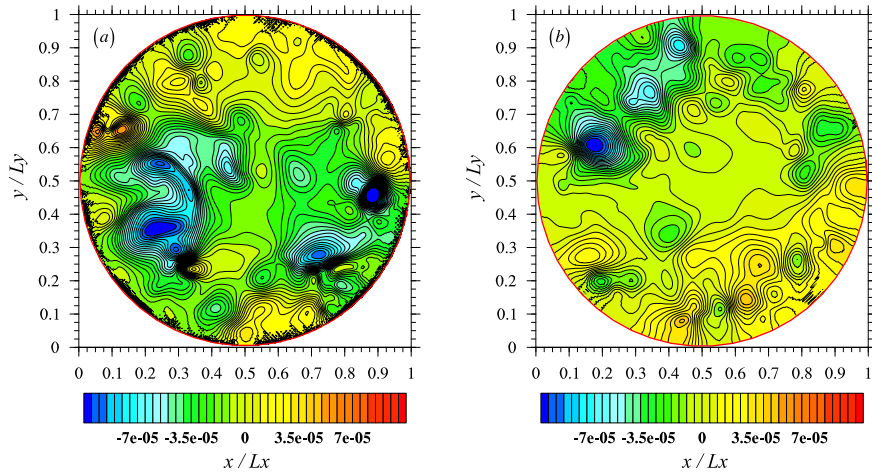
Fig. 12. An instantaneous snapshot of pressure contours at a given cross section (here $z = (N_z - 1)/2$), (*a*): D3Q19, (*b*): D3Q27.
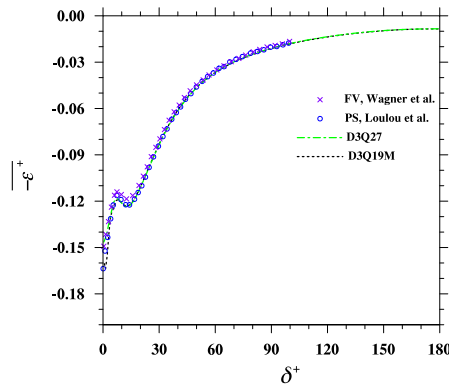
Fig. 13. Averaged dissipation rate profile.

rate is likely attributed to the much more severe pressure noise in the former, as compared in Fig. 12. The minor oscillation at $\delta^+ < 3$ in the D3Q19 result is due to the same reason.

Finally, the r.m.s. vorticity profiles in the streamwise, radial, and azimuthal directions are exhibited in Fig. 14. In our simulations, the vorticity components are calculated in the Cartesian coordinates based on a second-order central difference approximation and then projected to the cylindrical coordinates. For the boundary nodes, special treatment is necessary to maintain the same accuracy of vorticity calculation in the whole field when straight forward central difference scheme does not apply (see the Appendix). As indicated in Fig. 14, in general, the r.m.s. vorticity profiles of LBM simulations match well with the benchmark results, with only slight deviations in the region very close to the pipe wall. In the near wall region, the vorticity changes rapidly, which may require a better grid resolution to capture such change, a more accurate scheme to calculate vorticity, as well as a better binning strategy when converting the original data from Cartesian coordinate to the cylindrical coordinate. In Fig. 14 we also present the r.m.s. vorticity profiles from the classical PS DNS of turbulent channel flow [37]. The very similar profiles imply the similar vortical structures in the two flows.

4.3. High-order statistics in physical space

The skewness and flatness profiles of the velocity fluctuation in each direction are also calculated. The skewness $S\left(u'_\alpha\right)$ and flatness $F\left(u'_\alpha\right)$ are defined as

$$S\left(u'_\alpha\right) = \frac{\overline{u'^3_\alpha}}{\overline{u'^2_\alpha}^{3/2}}, \qquad F\left(u'_\alpha\right) = \frac{\overline{u'^4_\alpha}}{\overline{u'^2_\alpha}^{2}}. \tag{9}$$

As shown in Fig. 15, for streamwise velocity fluctuation, the LBM skewness profiles match well with the PS benchmark result, especially for the near wall region. For the radial velocity fluctuation, the LBM skewness results share similar trend of changing from positive values to negative values approaching to the pipe wall, as in the PS result. However, due to the pressure noise generated from the moving pipe wall, the D3Q19 result has an unphysical jump right at the pipe wall, which
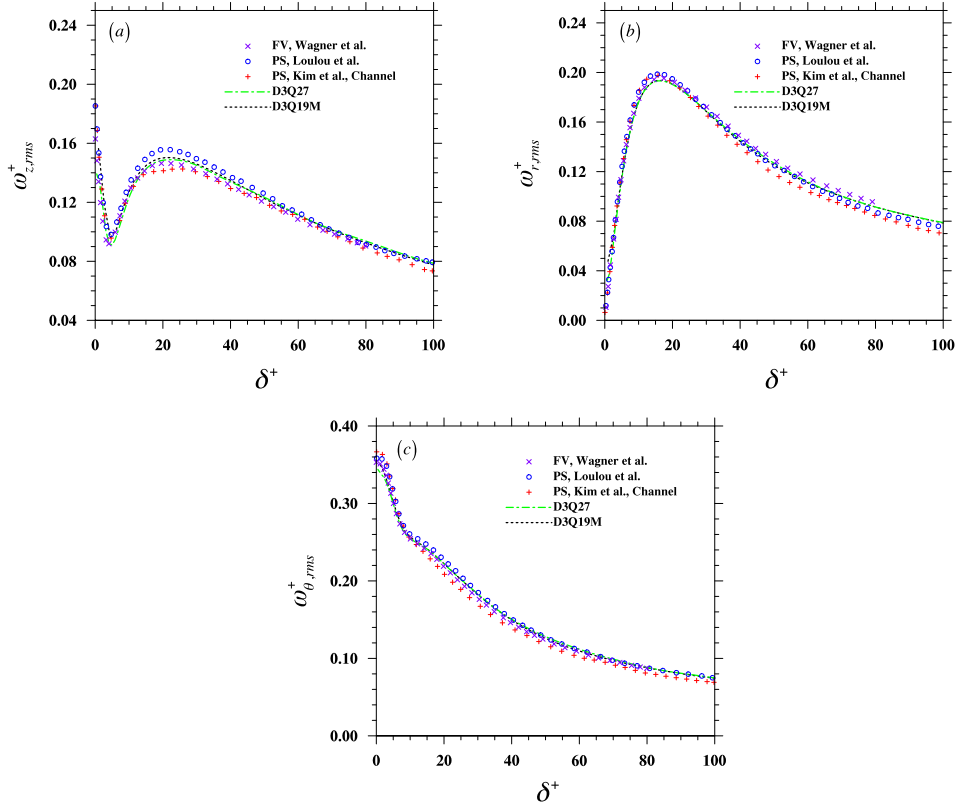
Fig. 14. Profiles of the r.m.s. vorticity fluctuations: (*a*) streamwise vorticity, (*b*) radial vorticity, (*c*) tangential vorticity.

is not observed in the D3Q27 simulation with static wall. In the azimuthal direction, the skewness should be identically zero since the flow has no preference in the azimuthal direction. This feature is better captured by the two LBM simulations than the other results. In that sense, our LBM results could be *even more* trustworthy than the PS result as the PS skewness in the azimuthal direction oscillates more significantly from zero. This could be a result of the insufficient time duration to average out the deviations in the PS simulation by Loulou et al. According to [10], the PS statistics are averaged over 46 fields at different times spanning 5.82 large eddy turnover times (defined as R/u_τ). In our simulation, a much longer period (with 2300 snapshots covering 60.1 large eddy turnover times) was used. Due to the stronger fluctuations of high order statistics, it usually requires a longer averaging period to reduce the uncertainty. The LBM flatness profiles are also in good agreements with the PS benchmark data, as shown in Fig. 16, except for a thin layer very close to the wall. The D3Q19 flatnesses of streamwise and radial velocities in this region exhibit small jumps, which are again a result of contamination by the acoustic waves near the moving pipe wall.

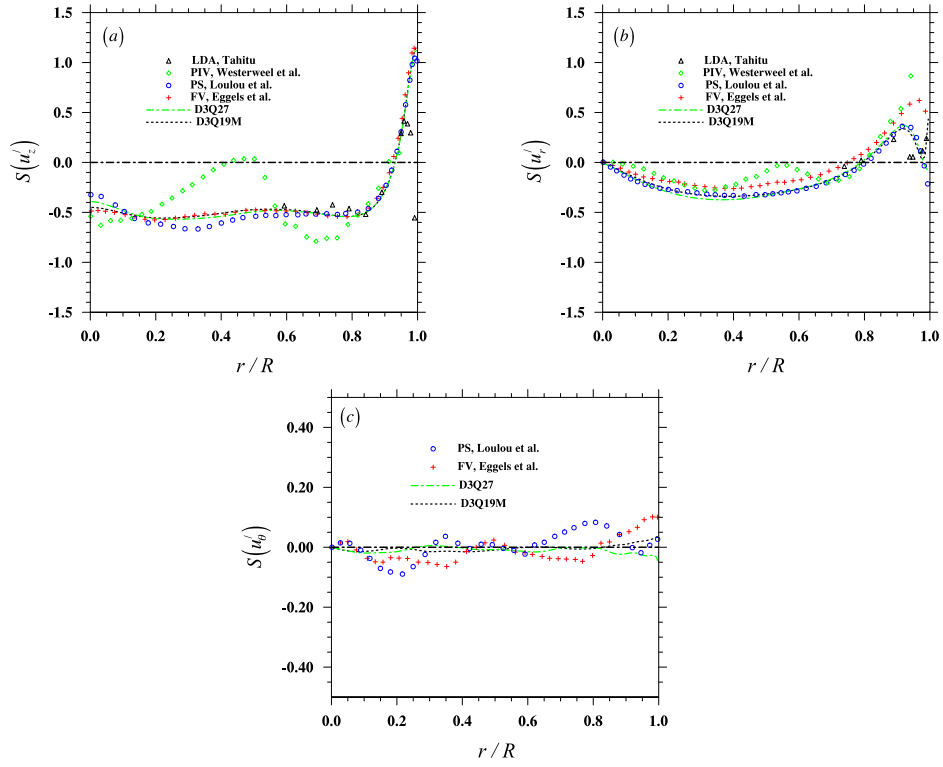### 4.4. Statistics in spectral space and analyses of flow length scales

To better quantify the flow scales in the turbulent pipe flow, we calculate the one-dimensional auto-correlation functions and energy spectra for all velocity and vorticity components at three selected radial locations $\delta^+ \approx 3.5$, $\delta^+ \approx 22.0$ and $\delta^+ \approx 122.0$, which correspond to the viscous sublayer, buffer region and logarithmic region, respectively. The auto-correlation functions are calculated in physical space, as

$$Q_{\alpha\alpha}(\delta_z, r) = \frac{\overline{u'_\alpha(r, z, \theta)\, u'_\alpha(r, z+\delta_z, \theta)}}{u^2_{\alpha,rms}(r)}, \tag{10a}$$
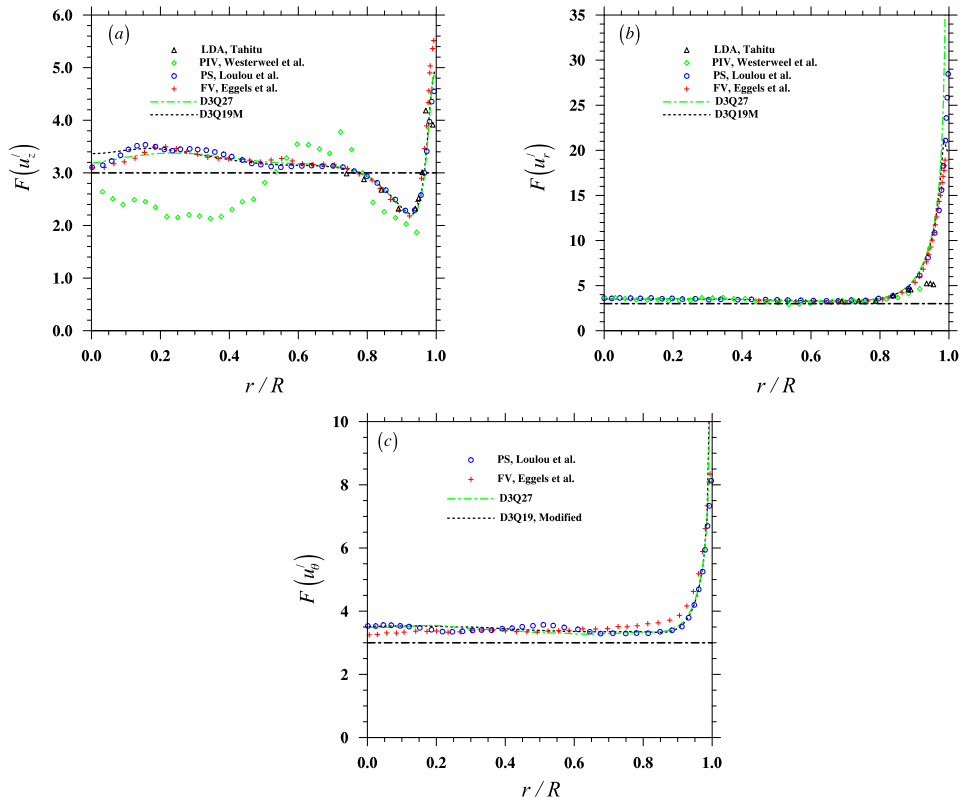
$$Q_{\alpha\alpha}(\delta_\theta, r) = \frac{\overline{u'_\alpha(r, z, \theta)\, u'_\alpha(r, z, \theta+\delta\theta)}}{u^2_{\alpha,rms}(r)}, \tag{10b}$$

where $\overline{(...)}$ denotes averaging over the azimuthal (or streamwise) direction and over time. The streamwise and azimuthal energy spectra are given as
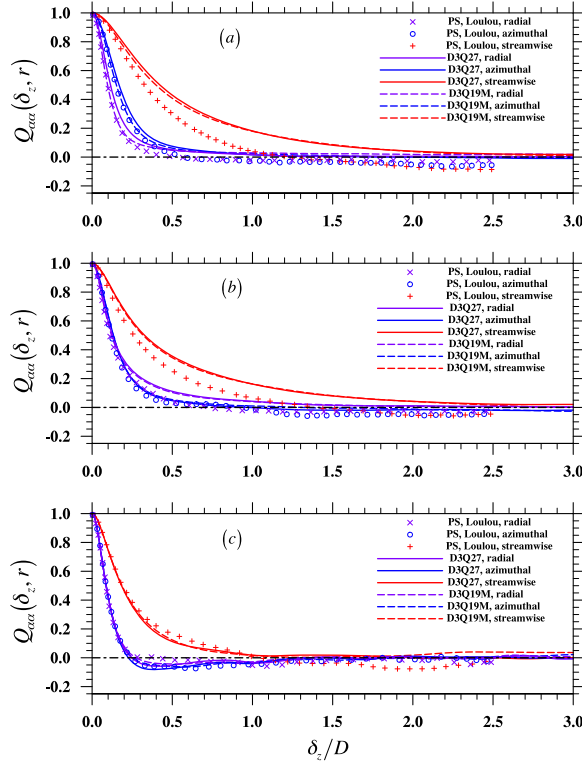
$$E_\alpha(k_z; r) = \frac{1}{2} \sum_{k_\theta} \left[\hat{u}_\alpha(r, k_\theta, k_z)\, \hat{u}^*_\alpha(r, k_\theta, k_z) + \hat{u}_\alpha(r, k_\theta, -k_z)\, \hat{u}^*_\alpha(r, k_\theta, -k_z) \right] \tag{11a}$$

Fig. 15. The skewness profiles of velocity components: (*a*) streamwise velocity, (*b*) radial velocity, and (*c*) azimuthal velocity.

Fig. 16. The flatness profiles of velocity components: (*a*) streamwise velocity, (*b*) radial velocity, and (*c*) azimuthal velocity.

Fig. 17. The streamwise two-point auto-correlation functions for velocity components at different locations, (*a*): near wall ($\delta^+ = 3.5$), (*b*): buffer region ($\delta^+ = 22.0$), (*c*): logarithmic region ($\delta^+ = 122.0$). FV results [9] are taken at slight different representative radial locations, as $\delta^+ \approx 4$, $\delta^+ \approx 17$ and $\delta^+ \approx 91$ in (*a*), (*b*) and (*c*), respectively.

$$E_\alpha \left(k_\theta; r\right) = \frac{1}{2} \sum_{k_z} \left[\hat{u}_\alpha \left(r, k_\theta, k_z\right) \hat{u}_\alpha^* \left(r, k_\theta, k_z\right) + \hat{u}_\alpha \left(r, -k_\theta, k_z\right) \hat{u}_\alpha^* \left(r, -k_\theta, k_z\right) \right] \tag{11b}$$

where $\hat{u}_\alpha \left(r, k_\theta, k_z\right)$ is the velocity or vorticity component in the Fourier space, which is defined as

$$\hat{u}_\alpha \left(r, k_\theta, k_z\right) = \frac{1}{N_z} \frac{1}{N_\theta} \sum_j \sum_k u_\alpha \left(z_k, \theta_j, r\right) \exp\left(-i\frac{2\pi k_z \cdot z_k}{L_z} - ik_\theta \cdot \theta_j \right) \tag{12}$$

and $\hat{u}_\alpha^* \left(r, k_\theta, k_z\right)$ is its complex conjugate.

As shown in Fig. 17, for the logarithmic region (Fig. 17(c)), the LBM results of two-point auto-correlation functions of azimuthal and radial velocity are in good agreement with corresponding PS results. However, for the two near wall locations (Fig. 17(a) and 17(b)), significant differences are observed for the streamwise velocity component between the PS and LBM correlation functions, as the latter decay much slower than the former. It is also noted that the PS auto-correlation functions for three velocity components are slightly negative, even at the largest separation distance $\delta_z = 2.5D$. Such behavior makes these PS results questionable since at the largest separation, the velocity components should be uncorrelated if the pipe length is sufficient to eliminate the effect of periodic boundary condition in the streamwise direction. Chin et al. [13] investigated the sufficient pipe length for converged turbulence statistics at different radial locations. Their result (Fig. 4a in [13]) suggests for $Re_\tau = 170$, a sufficient pipe length for the statistics of near wall region is $4\pi D$. In that sense, neither the pipe length in our LBM simulations (6.06D) nor the PS simulation of Loulou et al. (5D) is fully sufficient. However, the PS simulation of Loulou et al. is more affected by the insufficient pipe length, since its negative velocity correlation at large separation distances in the near-wall region was not reported by Chin et al. The significant derivations between the PS and the LBM correlation functions of the streamwise velocity component can be also explained by the insufficient pipe length used in our LBM simulation and the PS simulation by Loulou et al. The use of periodic boundary condition in the pipe length direction forces the streamwise velocity fluctuation to decorrelate. Since the PS simulation has shorter pipe length (5D) than our simulation (6.06D), the correlation function in the former tends to decay faster than that in the latter. Away from the wall the required pipe length decreases [13]. Thus the pipe lengths in both Loulou et al.'s PS simulation and our simulation become sufficient, a good agreement is therefore achieved.

For the vorticity components, the streamwise spatial correlations are shown in Fig. 18. Although all results are in good qualitative agreements, significant quantitative differences can be observed between the PS correlation functions and their
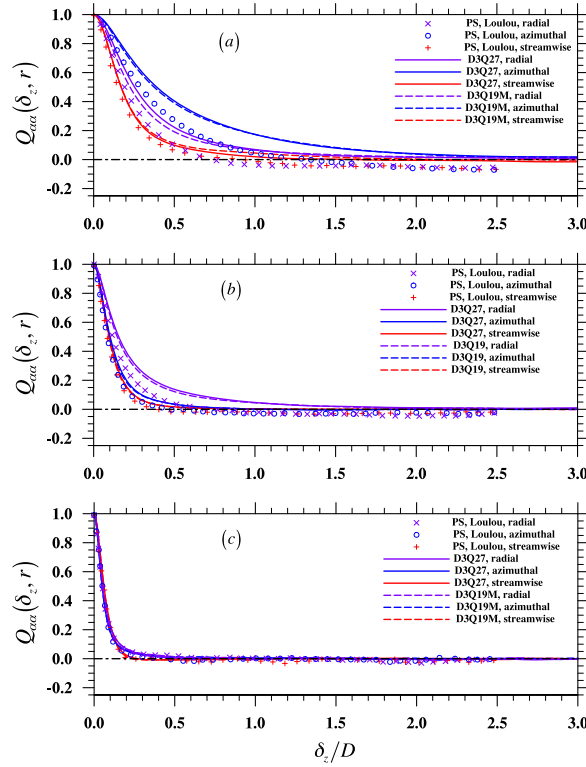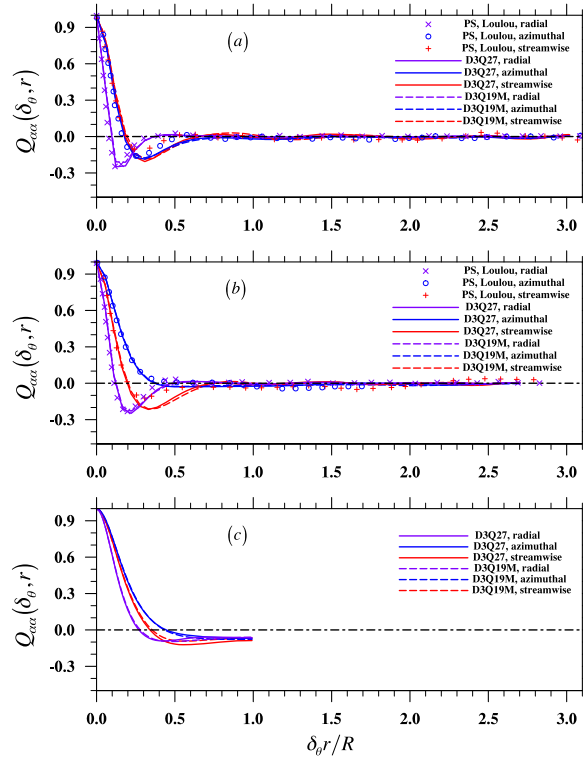
Fig. 18. The streamwise two-point auto-correlation functions for vorticity components at different locations, (*a*): near wall ($\delta^+ = 3.5$), (*b*): buffer region ($\delta^+ = 22.0$), (*c*): logarithmic region ($\delta^+ = 122.0$).

LBM counterparts, especially in the near-wall region. Again, such differences are likely due to the inadequate pipe length used in both PS simulation and our LBM simulations. Away from the wall, the vortex structures are more isotropic, as the correlation functions of three vorticity components essentially overlap.
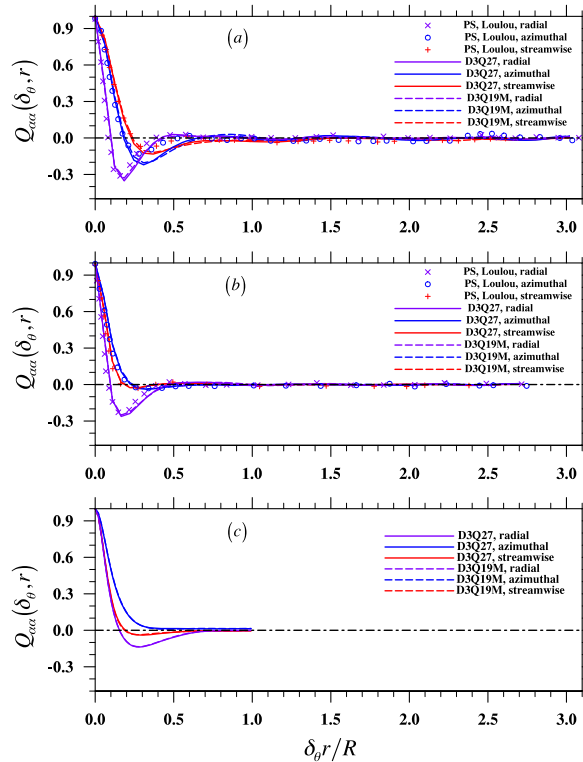
The azimuthal correlation functions from LBM and PS are shown in Fig. 19 and Fig. 20 for velocity and vorticity, respectively. In these cases, the PS data are only available for the near-wall and buffer regions. Here, the PS correlations for velocity and vorticity components do decay to zero as the azimuthal separation is increased. In general, the LBM results of the D3Q19 and D3Q27 simulations are in good agreements, they also match the PS results as well.

The one-dimensional energy spectra in both streamwise and azimuthal directions for all velocity and vorticity components are presented in Fig. 21 to Fig. 24 at the same selected radial locations. In order to compare with the benchmark results, we rescaled the PS benchmark dataset by multiplying a factor $\sum_{k_z \text{ or } k_\theta} E_{\alpha, LBM} / \sum_{k_z \text{ or } k_\theta} E_{\alpha, PS}$ such that the areas under the pair are the same. In the near wall region (Fig. 21(a) and Fig. 22(a)), the D3Q27 energy spectra at small wavenumbers are in better agreements with the PS results than those from the D3Q19 simulation. This is mainly because that the D3Q27 simulation uses static wall and is less contaminated by the pressure noises. The streamwise spectra of LBM simulations also slightly deviate from the PS results in the logarithmic region (Fig. 21(c) and Fig. 22(c)). This is likely because the number of data points near the pipe center in the LBM simulations are small, since the LBM simulations use Cartesian grid. Other than these, the streamwise energy spectra obtained from the two LBM simulations are in good agreement with the PS benchmark curves for all velocity and vorticity components.

Compared to the streamwise spectra, the deviations in the azimuthal spectra are more significant between the LBM and PS simulations. These derivations are likely because of the insufficient number of bins in the azimuthal direction used in data conversion from the Cartesian to cylindrical coordinates. In the LBM simulations we use 100 equal-size bins in the azimuthal direction in the data conversion. The energy spectra for both velocity and vorticity components confirm the nearly isotropic flow in the pipe center. It is particularly interesting to observe an unphysical peak in the D3Q19 azimuthal spectrum of the azimuthal velocity at $k_\theta = 4$ in the near wall region (Fig. 23(a)). The same unphysical peak is also exhibited in the azimuthal spectra of streamwise vorticity component in the D3Q19 simulation (Fig. 24(a)). These unphysical peaks at $k_\theta = 4$ are related to the secondary flow pattern caused by the use of D3Q19 lattice, as reported in [19,6,18]. On the other hand, no such peak is present in the D3Q27 energy spectra, confirming that the D3Q27 lattice grid tends to lead to much smaller secondary flow in the simulations. Compared with the significant secondary flow that reported in the previous LES study [6], the secondary flow observed in the present D3Q19 simulation is much weaker. In Fig. 25(a) we show the cross-sectional contour of the averaged streamwise velocity over about 44.6 large eddy turnover times. Although a weak secondary flow pattern can be still observed, the velocity contour generally has no obvious azimuthal dependence. The much weaker secondary flow due
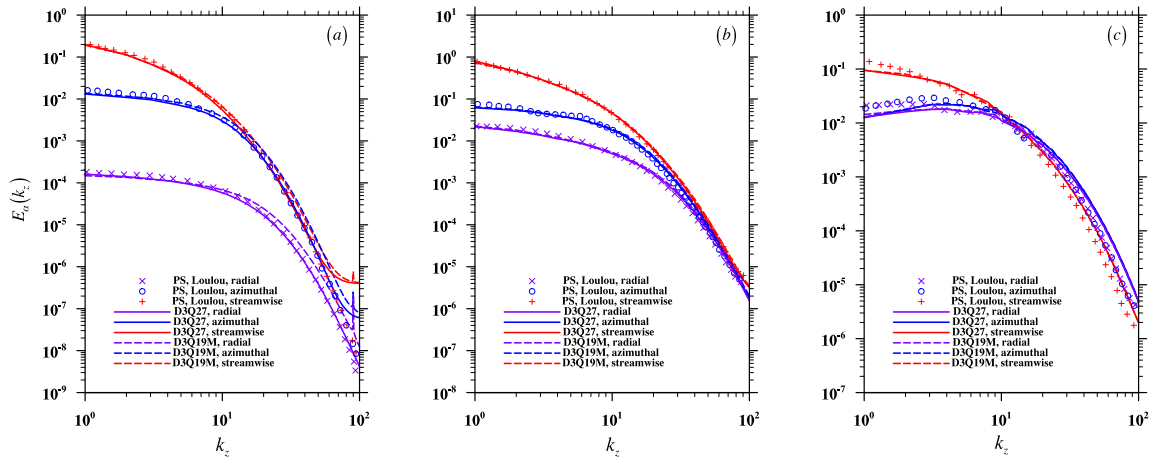
Fig. 19. The azimuthal two-point auto-correlation functions for velocity components at different locations, (*a*): near wall ($\delta^+ = 3.5$), (*b*): buffer region ($\delta^+ = 22.0$), (*c*): logarithmic region ($\delta^+ = 122.0$).
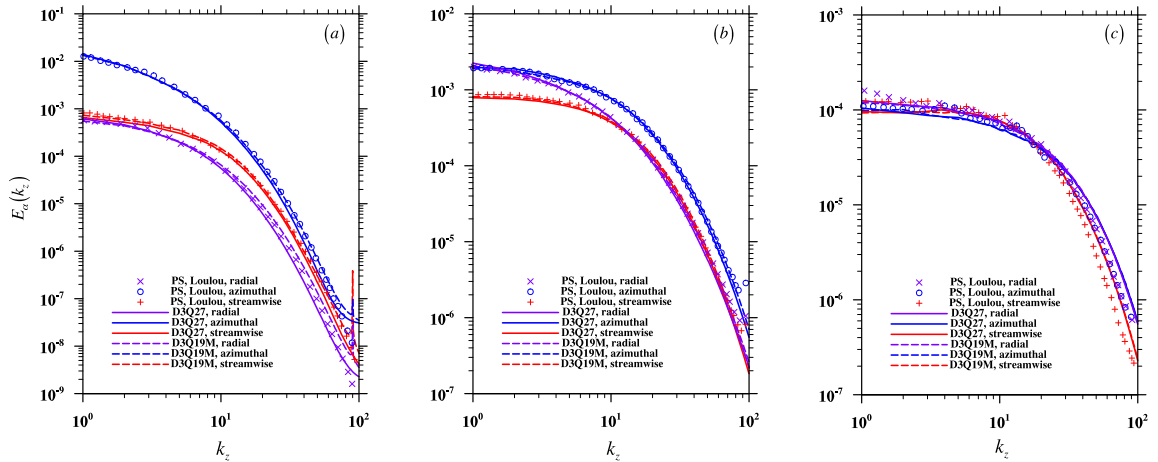

Fig. 20. The azimuthal two-point auto-correlation functions for vorticity components at different locations, (*a*): near wall ($\delta^+ = 3.5$), (*b*): buffer region ($\delta^+ = 22.0$), (*c*): logarithmic region ($\delta^+ = 122.0$).

Fig. 21. The streamwise energy spectra for velocity components at different locations, (*a*): near wall ($\delta^+ = 3.5$), (*b*): buffer region ($\delta^+ = 22.0$), (*c*): logarithmic region ($\delta^+ = 122.0$). FV results [9] are taken at slight different representative radial locations, as $\delta^+ \approx 4$, $\delta^+ \approx 17$ and $\delta^+ \approx 91$ in (*a*), (*b*) and (*c*), respectively.

Fig. 22. The streamwise energy spectra for vorticity components at different locations, (*a*): near wall ($\delta^+ = 3.5$), (*b*): buffer region ($\delta^+ = 22.0$), (*c*): logarithmic region ($\delta^+ = 122.0$).

Fig. 23. The azimuthal energy spectra for velocity components at different locations, (*a*): near wall ($\delta^+ = 3.5$), (*b*): buffer region ($\delta^+ = 22.0$), (*c*): logarithmic region ($\delta^+ = 122.0$).
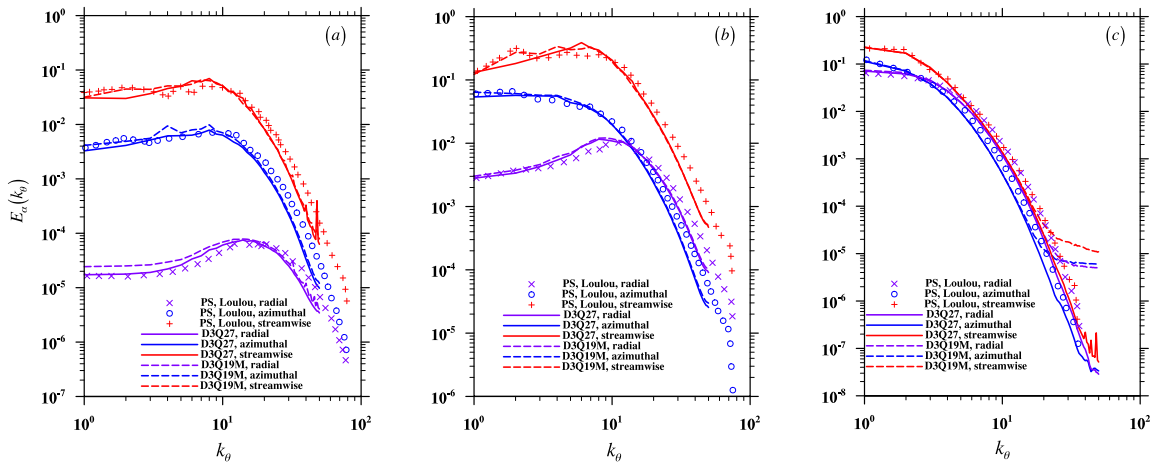
Fig. 24. The azimuthal energy spectra for vorticity components at different locations, (a): near wall ($\delta^+ = 3.5$), (b): buffer region ($\delta^+ = 22.0$), (c): logarithmic region ($\delta^+ = 122.0$).
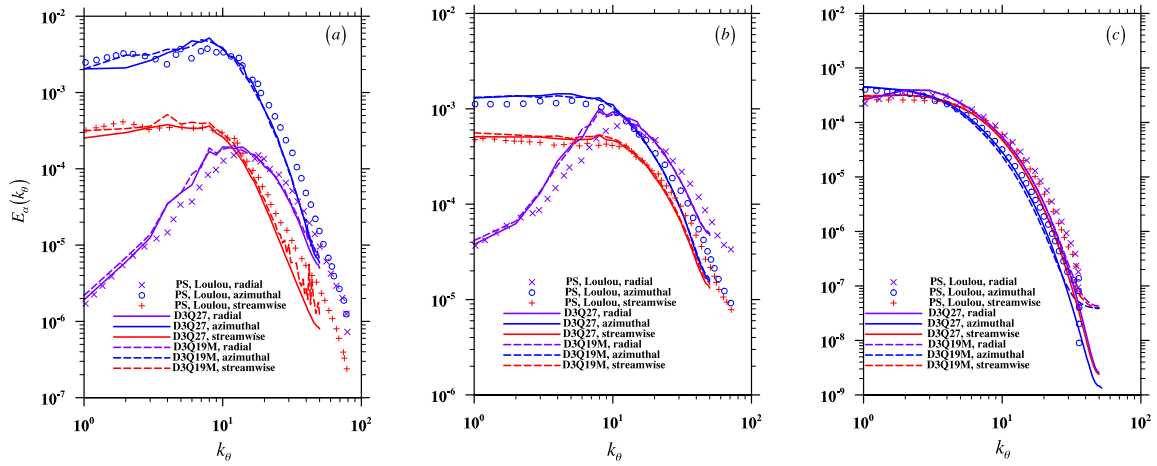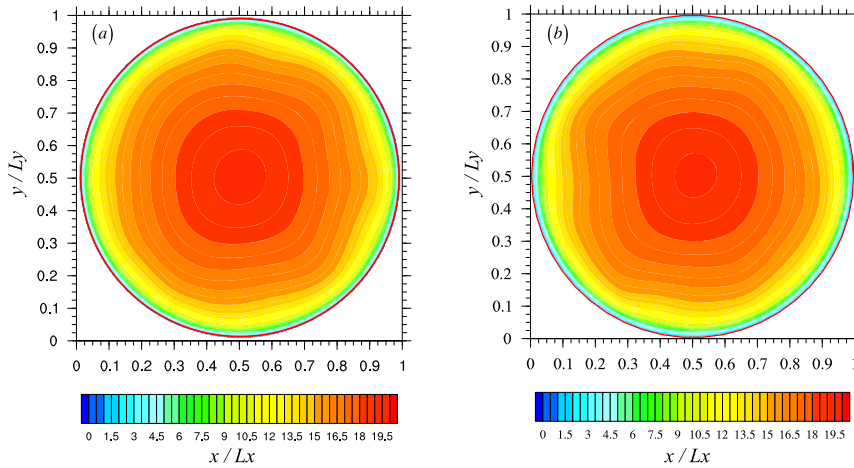

Fig. 25. Contours for averaged streamwise velocity. The averaging is taken over the streamwise direction and over time. Here a duration of 44.6 eddy turnover times were used for the D3Q19 result on the left, and 28.5 eddy turnover times were used for the D3Q27 result on the right.

to numerical artifact in our D3Q19 LBM simulation is due to several factors: first, we shift the pipe center a little bit so the lattice arrangement is no longer perfectly symmetric; second, compared with [6] who used only 100 lattice units for the pipe diameter, our resolution is three times better; finally, our improved boundary implementation may also reduce such artifact. For completeness, a similar contour plot in the D3Q27 simulation that averaged over 28.5 large eddy turnover times is shown in Fig. 25(b). No obvious superiority is observed in terms of suppressing the artificial secondary flows when compared to the corresponding D3Q19 result.

5. Summary and conclusions

In this work, we present a direct numerical simulation of a fully developed turbulent pipe flow at the bulk flow Reynolds number $Re_b \approx 5300$ (or $Re_\tau = 180$), using the lattice Boltzmann method on both D3Q19 and D3Q27 lattices. A number of difficulties associated with accuracy and numerical instability of LBM involving a curved wall have been resolved, especially for the D3Q19 simulation, to make the simulations possible for the first time. To handle this turbulent flow with reasonable computational resources, for the D3Q19 simulation, an extended MRT LBM model has been introduced to improve the numerical stability of the simulation by relaxing the strict relationship between the viscosities and relaxation parameters in standard LBM. To accelerate the transition from laminar to turbulence, a divergence free perturbation force field is introduced to excite the flow field at the early stages. The simulation set-up and other implementation details have also been presented. Compared with the turbulent channel flow simulation, we discovered a more strict Ma constraint in the D3Q19 simulation due to the presence of a strong checkerboard instability. To overcome this problem, we added a negative velocity to the pipe wall to reduce the velocity magnitude in the center region of the pipe. This novel treatment however, brings another issue related to the violation of Galilean invariance on the pipe wall surface. This issue is resolved by an improved

bounce back scheme based on coordinate transformation. Although the same checkerboard instability problem does not appear in our current D3Q27 simulation, the difficulties and solutions discussed for the D3Q19 simulation are still useful for the D3Q27 simulations in more critical situations. We believe these implementation details in our work provide a useful guidance for others to conduct similar simulations in the future.

Next, the results from the LBM simulations are compared systematically with previous DNS and measurement data. We have demonstrated that the VGI error in the usual interpolated bounce back causes a significant error on the mean velocity, although this seems to have only a minor impact on the fluctuating velocity statistics. The VGI error on the mean velocity can be removed by using the improved bounce back based on coordinate transformation. The comparisons in the r.m.s. velocities, using the spectral simulation data [10] as the benchmark, reveal that the LBM results are more accurate than the second-order finite difference results on a uniform grid. LBM treats the advection in the mesoscopic space exactly (except when the interpolated bounce-back is used near the curved wall) and preserves the exact local mass and momentum conservations, which could be physically more accurate than the second-order FV method based on solving the Navier–Stokes equations. Therefore, we argue that the early DNS data by Eggels et al. are rather inaccurate and should not be used as a benchmark in the future. Previously, the DNS data by Eggels et al. have often been used as a benchmark, for example, in [6], [18] and [47]. The comparisons of more sensitive statistics, such as r.m.s. vorticity and higher-order statistics (skewness, flatness) of velocity fluctuations again confirm LBM can serve as a reliable tool for the DNS simulations of flows in a cylindrical domain.

Our study demonstrates that both D3Q19 and D3Q27 simulations are capable to provide accurate flow statistics in a turbulent pipe flow simulation. Although the direct comparisons between the two sets of results do reveal several advantages of using D3Q27 lattice. For example, the moving frame of reference used in the D3Q19 simulation to enhance numerical stability causes pressure noises near the pipe wall which contaminate the pressure fluctuation and high-order velocity statistics in a region very close to the wall (within roughly 3 grid spacings from the wall). This indicates that the novel moving boundary treatment used in this paper is by no means perfect. The weak unphysical energy peaks at $k_\theta = 4$ appear in the azimuthal energy spectra of tangential velocity and streamwise vorticity confirm the existence of unphysical secondary flow related to the use of D3Q19 lattice *aka*, the lattice effect [19,6,18]. This problem can be avoided by the using the D3Q27 lattice. However, we demonstrate that this artifact in our D3Q19 simulation is much weaker than those found in the previous LES study by Kang & Hassan [6], namely, the mean velocity profile in our LBM deviates from the spectral benchmark by less than 1%, compared to 28% in [6]. This dramatic improvement is related to several reasons: the shifting of lattice nodes relative to the pipe center, use of fine grid resolution, and the improved implementation of boundary condition. Therefore, we conclude that given a sufficient grid resolution and careful implementations, both D3Q19 and D3Q27 can be used for turbulent pipe flow simulations in LBM.

Acknowledgements

Appendix A

A.1. The D3Q27 MRT model

In the D3Q27 MRT model, twenty-seven three-dimensional lattice velocities are used and they are

$$\mathbf{e}_i = \begin{cases} (0,0,0)\,c, & i = 0, \\ (\pm 1,0,0)\,c, \quad (0,\pm 1,0)\,c, \quad (0,0,\pm 1)\,c, & i = 1,2,\ldots,6, \\ (\pm 1,\pm 1,0)\,c, \quad (\pm 1,0,\pm 1)\,c, \quad (0,\pm 1,\pm 1)\,c, & i = 7,8,\ldots,18, \\ (\pm 1,\pm 1,\pm 1)\,c, & i = 19,20,\ldots,26, \end{cases} \tag{13}$$

where $c = \delta_x/\delta_t$, δ_x and δ_t are the grid spacing and time step size, respectively. The moment vector $\mathbf{m}$ therefore contains twenty-seven moments. These moments are constructed in an ascending manner according to their order, as shown in Table 5. The corresponding equilibrium moments in $\mathbf{m}^{(eq)}$ are functions of only the conserved moments, *i.e.*, density fluctuation $\delta\rho$ and momentum $\rho_0\mathbf{u}$.[2] They are

---

[2] Note that, here we follow the incompressible formulation proposed in [48], where density is partitioned into a local density fluctuation $\delta\rho$ and a constant background density ρ_0.

Table 5
The definition of moments in the D3Q27 MRT model. Here the subscripts α, β, and γ denote the spatial direction.

Moment index	Order	Definition	Physical representation
0	0	$\langle f \mid \|\mathbf{e}\|^0 \rangle$	Mass density
1–3	1	$\langle f \mid e_\alpha \rangle$	Momentum in α
4	2	$\langle f \mid \|\mathbf{e}\|^2 - 2 \rangle$	Kinetic energy
5–6	2	$\langle f \mid 3e_x^2 - \|\mathbf{e}\|^2 \rangle$, $\langle f \mid e_y^2 - e_z^2 \rangle$	Normal stress
7–9	2	$\langle f \mid e_\alpha e_\beta \rangle$, $\alpha \neq \beta$	Shear stress
10–12	3	$\langle f \mid (3\|\mathbf{e}\|^2 - 7) e_\alpha \rangle$	Energy flux in α
13–15	3	$\langle f \mid e_\alpha \left(e_\beta^2 - e_\gamma^2\right) \epsilon_{\alpha\beta\gamma} \rangle$	Normal stress flux
16	3	$\langle f \mid e_x e_y e_z \rangle$	Shear stress flux
17	4	$\langle f \mid 3\|\mathbf{e}\|^4 - 11\|\mathbf{e}\|^2 + 8 \rangle$	Energy square
18	4	$\langle f \mid (3\|\mathbf{e}\|^2 - 5)\left(3e_x^2 - \|\mathbf{e}\|^2\right) \rangle$	Energy normal stress coupling
19	4	$\langle f \mid (3\|\mathbf{e}\|^2 - 5)\left(e_y^2 - e_z^2\right) \rangle$	Energy normal stress coupling
20–22	4	$\langle f \mid (3\|\mathbf{e}\|^2 - 8) e_\alpha e_\beta \rangle$, $\alpha \neq \beta$	Energy shear stress coupling
23–25	5	$\langle f \mid \left(\frac{9}{2}\|\mathbf{e}\|^4 - \frac{39}{2}\|\mathbf{e}\|^2 + 19\right) e_\alpha \rangle$	Energy square flux in α
26	6	$\langle f \mid \frac{9}{2}\|\mathbf{e}\|^6 - \frac{45}{2}\|\mathbf{e}\|^4 + 30\|\mathbf{e}\|^2 - 8 \rangle$	Energy cube

$$
\begin{aligned}
& m_0^{(eq)} = \delta\rho, \ \ m_1^{(eq)} = \rho_0 u, \ \ m_2^{(eq)} = \rho_0 v, \ \ m_3 = \rho_0 w, \\
& m_4^{(eq)} = -\delta\rho + \rho_0 \left(u^2 + v^2 + w^2\right), \ \ m_5^{(eq)} = \rho_0 \left(2u^2 - v^2 - w^2\right), \\
& m_6^{(eq)} = \rho_0 \left(v^2 - w^2\right), \ \ m_7^{(eq)} = \rho_0 uv, \ \ m_8^{(eq)} = \rho_0 uw, \ \ m_9^{(eq)} = \rho_0 vw, \\
& m_{10}^{(eq)} = -2\rho_0 u, \ \ m_{11}^{(eq)} = -2\rho_0 v, \ \ m_{12}^{(eq)} = -2\rho_0 w, \\
& m_{13}^{(eq)} = m_{14}^{(eq)} = m_{15}^{(eq)} = m_{16}^{(eq)} = 0, \ \ m_{17}^{(eq)} = \alpha_{17}\delta\rho + \beta_{17}\rho_0 \left(u^2 + v^2 + w^2\right), \\
& m_{18}^{(eq)} = \beta_{18}\rho_0 \left(2u^2 - v^2 - w^2\right), \ \ m_{19}^{(eq)} = \beta_{19}\rho_0 \left(v^2 - w^2\right), \\
& m_{20}^{(eq)} = \gamma_{20}\rho_0 uv, \ \ m_{21}^{(eq)} = \gamma_{21}\rho_0 vw, \ \ m_{22}^{(eq)} = \gamma_{22}\rho_0 uw, \ \ m_{23}^{(eq)} = \zeta_{23}\rho_0 u, \\
& m_{24}^{(eq)} = \zeta_{24}\rho_0 v, \ \ m_{25}^{(eq)} = \zeta_{25}\rho_0 w, \ \ m_{26}^{(eq)} = \alpha_{26}\delta\rho + \beta_{26}\rho_0 \left(u^2 + v^2 + w^2\right),
\end{aligned}
\tag{14}
$$

where $\mathbf{u} = (u, v, w)$ is the local velocity. α_{17}, β_{17}, β_{18}, β_{19}, γ_{20}, γ_{21}, γ_{22}, ζ_{23}, ζ_{24}, ζ_{25}, α_{26}, β_{26} are coefficients of fourth- or higher-order equilibrium moments that are irrelevant to the derivation of the N–S equations. In our simulation we choose $\alpha_{17} = 2$, $\beta_{17} = -4$, $\beta_{18} = \beta_{19} = -1$, $\gamma_{20} = \gamma_{21} = \gamma_{22} = -1$, $\zeta_{23} = \zeta_{24} = \zeta_{25} = 1$, $\alpha_{26} = -1$, $\beta_{26} = 3$ to be consistent with the LBGK equilibrium, for simplicity.

The mesoscopic external force vector $\boldsymbol{\Psi}$ in D3Q27 MRT model can be designed via an inverse design analysis in the moment space [49]. The relevant elements of $\boldsymbol{\Psi}$ in terms of the N–S equations are summarized as

$$
\begin{aligned}
& \Psi_0 = 0, \ \ \Psi_1 = \left(1 - \tfrac{s_1}{2}\right) F_x \delta_t, \ \ \Psi_2 = \left(1 - \tfrac{s_2}{2}\right) F_y \delta_t, \ \ \Psi_3 = \left(1 - \tfrac{s_3}{2}\right) F_z \delta_t, \\
& \Psi_4 = -(2 - s_4)\left(uF_x + vF_y + wF_z\right), \ \ \Psi_5 = -(2 - s_5)\left(2uF_x - vF_y - wF_z\right), \\
& \Psi_6 = -(2 - s_6)\left(vF_y - wF_z\right), \ \ \Psi_7 = \left(1 - \tfrac{s_7}{2}\right)\left(uF_y + vF_x\right), \\
& \Psi_8 = \left(1 - \tfrac{s_8}{2}\right)\left(vF_z + wF_y\right), \ \ \Psi_9 = \left(1 - \tfrac{s_9}{2}\right)\left(uF_z + wF_x\right),
\end{aligned}
\tag{15}
$$

where $\mathbf{F} = (F_x, F_y, F_z)$ is the macroscopic force per unit mass. s_i is the relaxation parameter of moment m_i. In this D3Q27 MRT model, the relaxation parameter of the energy mode, *i.e.*, s_4, is related to the bulk viscosity ν^V in the resulting N–S equations, while the relaxation parameters of the normal and shear stress modes, *i.e.*, s_5 to s_9 are related to the shear viscosity ν, as

$$
\nu^V = \frac{2}{9}\left(\frac{1}{s_4} - \frac{1}{2}\right) c^2 \delta_t,
\tag{16a}
$$

$$
\nu = \frac{1}{3}\left(\frac{1}{s_5} - \frac{1}{2}\right) c^2 \delta_t, \ \ s_5 = s_6 = s_7 = s_8 = s_9.
\tag{16b}
$$

The other mesoscopic forcing terms are irrelevant to macroscopic body force term in the N–S equations. They are simply set to zero in our simulation.

A.1.1. The D3Q19 extended MRT model

When the D3Q19 lattice grid is used, an extended MRT LBM model is adopted to enhance the numerical stability. Same as the standard D3Q19 MRT model [34], the nineteen lattice velocities $\mathbf{e}_i$ are

$$
\mathbf{e}_i = \begin{cases} (0, 0, 0)\,c, & i = 0, \\ (\pm 1, 0, 0)\,c, \ (0, \pm 1, 0)\,c, \ (0, 0, \pm 1)\,c, & i = 1, 2, \ldots, 6, \\ (\pm 1, \pm 1, 0)\,c, \ (\pm 1, 0, \pm 1)\,c, \ (0, \pm 1, \pm 1)\,c, & i = 7, 8, \ldots, 18. \end{cases}
\tag{17}
$$

Table 6
The definitions of moments in a D3Q19 MRT model.

Moment index	Order	Definition	Physical representation
0	0	$\langle f \mid \|\mathbf{e}\|^0 \rangle$	Mass density
1–3	1	$\langle f \mid e_\alpha \rangle$	Momentum in α
4	2	$\langle f \mid 19\|\mathbf{e}\|^2 - 30 \rangle$	Kinetic energy
5–6	2	$\langle f \mid 3e_x^2 - \|\mathbf{e}\|^2 \rangle, \langle f \mid e_y^2 - e_z^2 \rangle$	Normal stress
7–9	2	$\langle f \mid e_\alpha e_\beta \rangle, \alpha \neq \beta$	Shear stress
10–12	3	$\langle f \mid (5\|\mathbf{e}\|^2 - 9) e_\alpha \rangle$	Energy flux in α
13–15	3	$\langle f \mid e_\alpha \left(e_\beta^2 - e_\gamma^2\right) \epsilon_{\alpha\beta\gamma} \rangle$	Normal stress flux
16	4	$\langle f \mid \frac{21}{2}\|\mathbf{e}\|^4 - \frac{53}{2}\|\mathbf{e}\|^2 + 12 \rangle$	Energy square
17	4	$\langle f \mid (3\|\mathbf{e}\|^2 - 5)(3e_x^2 - \|\mathbf{e}\|^2) \rangle$	Energy normal stress coupling
18	4	$\langle f \mid (3\|\mathbf{e}\|^2 - 5)(e_y^2 - e_z^2) \rangle$	Energy normal stress coupling

The same number of moments are constructed as in Table 6. Unlike the standard MRT models, the equilibrium moment vector $\mathbf{m}^{(eq)}$ in this extended D3Q19 MRT model is formally written as

$$\mathbf{m}^{(eq)} = \mathbf{m}^{(eq,0)} + \mathbf{m}^{(eq,1)}, \tag{18}$$

where the first term $\mathbf{m}^{(eq,0)}$ can be viewed as the equilibrium moment vector in the standard MRT model [34].

$$\begin{aligned}
&m_0^{(eq,0)} = \delta\rho, \ m_1^{(eq,0)} = \rho_0 u, \ m_2^{(eq,0)} = \rho_0 v, \ m_3 = \rho_0 w, \\
&m_4^{(eq,0)} = -11\delta\rho + 19\rho_0\left(u^2 + v^2 + w^2\right), \ m_5^{(eq,0)} = \rho_0\left(2u^2 - v^2 - w^2\right), \\
&m_6^{(eq,0)} = \rho_0\left(v^2 - w^2\right), \ m_7^{(eq,0)} = \rho_0 uv, \ m_8^{(eq,0)} = \rho_0 uw, \ m_9^{(eq,0)} = \rho_0 vw, \\
&m_{10}^{(eq,0)} = -2\rho_0 u/3, \ m_{11}^{(eq,0)} = -2\rho_0 v/3, \ m_{12}^{(eq)} = -2\rho_0 w/3, \\
&m_{13}^{(eq,0)} = m_{14}^{(eq,0)} = m_{15}^{(eq,0)} = 0, \ m_{16}^{(eq,0)} = \alpha_{16}\delta\rho + \beta_{16}\rho_0\left(u^2 + v^2 + w^2\right), \\
&m_{17}^{(eq,0)} = \gamma_{17}\rho_0\left(2u^2 - v^2 - w^2\right), \ m_{18}^{(eq,0)} = \gamma_{18}\rho_0\left(2u^2 - v^2 - w^2\right),
\end{aligned} \tag{19}$$

where α_{16}, β_{16}, γ_{17} and γ_{18} are free parameters irrelevant to the derivation of the N–S equations. We choose $\alpha_{16} = 0$, $\beta_{16} = -475/63$ and $\gamma_{17} = \gamma_{18} = 0$ as suggested by d'Humières et al. [34]. They obtained those values via a linear stability analysis.

In additional to $\mathbf{m}^{(eq,0)}$, a second term $\mathbf{m}^{(eq,1)}$ is introduced into the equilibrium moments to alter the relationship between viscosities and relaxation parameters, *i.e.*, Eq. (16). This idea was first proposed by Inamuro [50] with a LBGK collision model. Since only the relaxation parameters of energy and five stress moments are related to the bulk and shear viscosities in the resulting N–S equations, as shown in Eq. (16), only the 6 elements out of the 19 in $\mathbf{m}^{(eq,1)}$, corresponding to the energy and stress moments, are relevant to this modification, and they are designed as

$$\begin{aligned}
&m_4^{(eq,1)} = \rho_0\zeta\left(\partial_x u + \partial_y v + \partial_z w\right), \ m_5^{(eq,1)} = \rho_0\lambda\left(4\partial_x u - 2\partial_y v - 2\partial_z w\right), \\
&m_6^{(eq,1)} = \rho_0\lambda\left(2\partial_y v - 2\partial_z w\right), \ m_7^{(eq,1)} = \rho_0\lambda\left(\partial_x v + \partial_y u\right), \\
&m_8^{(eq,1)} = \rho_0\lambda\left(\partial_y w + \partial_z v\right), \ m_9^{(eq,1)} = \rho_0\lambda\left(\partial_z u + \partial_x w\right),
\end{aligned} \tag{20}$$

where λ and ζ are two coefficients controlling the magnitude of the additional equilibrium moment $\mathbf{m}^{(eq,1)}$. The other elements in $\mathbf{m}^{(eq,1)}$ are simply set to zero. Using the Chapman–Enskog expansion, we can show that this extended model leads to the Navier–Stokes equations with the following shear and bulk viscosities [51]

$$\nu^V = \frac{2}{9}\left(\frac{1}{s_4} - \frac{1}{2}\right)c^2\delta_t - \zeta, \tag{21a}$$

$$\nu = \frac{1}{3}\left(\frac{1}{s_5} - \frac{1}{2}\right)c^2\delta_t - \lambda, \ s_5 = s_6 = s_7 = s_8 = s_9. \tag{21b}$$

Clearly, the introduction of $\mathbf{m}^{(eq,1)}$ into the equilibrium moments modifies the relationships between viscosities and corresponding relaxation parameters from Eq. (16) to Eq. (21). Even for small physical viscosities, there is no need to set the relaxation parameters s_{5-9} and s_4 too close to 2, due to the presence of non-zero λ and ζ. In the actual implementation, we find that the best stability can be achieved with $1.8 \leq s_{5-9} \leq 1.9$, while the value of s_4 is found to have no noticeable effect on the numerical stability.

Following the same inverse design procedure [49], the mesoscopic force vector $\mathbf{\Psi}$ for the D3Q19 MRT model is designed. Again, only 10 out of 19 are relevant to the N–S equations, they are

$$\Psi_0 = 0, \quad \Psi_1 = (1 - 0.5s_1) F_x, \quad \Psi_2 = (1 - 0.5s_2) F_y, \quad \Psi_3 = (1 - 0.5s_3) F_z,$$
$$\Psi_4 = 38 (1 - 0.5s_4) \left(uF_x + vF_y + wF_z \right), \quad \Psi_5 = 2 (1 - 0.5s_5) \left(2uF_x - vF_y - wF_z \right),$$
$$\Psi_6 = 2 (1 - 0.5s_6) \left(vF_y - wF_z \right), \quad \Psi_7 = (1 - 0.5s_7) \left(vF_x + uF_y \right),$$
$$\Psi_8 = (1 - 0.5s_8) \left(vF_z + wF_y \right), \quad \Psi_9 = (1 - 0.5s_9) \left(uF_z + wF_x \right). \tag{22}$$

The other elements of $\boldsymbol{\Psi}$ are set to zero.

It should be noted that all the relevant $\mathbf{m}^{(eq,1)}$ components in Eq. (20) can be calculated mesoscopically as

$$\rho_0 \left(\partial_x u + \partial_y v + \partial_z w \right) = \frac{G_4}{\left(\zeta - \frac{38c^2 \delta_t}{3s_4} \right)} \tag{23a}$$

$$\rho_0 \left(4\partial_x u - 2\partial_y v - 2\partial_z w \right) = \frac{G_5}{\left(\lambda - \frac{c^2 \delta_t}{3s_5} \right)} \tag{23b}$$

$$\rho_0 \left(2\partial_y v - 2\partial_z w \right) = \frac{G_6}{\left(\lambda - \frac{c^2 \delta_t}{3s_6} \right)} \tag{23c}$$

$$\rho_0 \left(\partial_x v + \partial_y u \right) = \frac{G_7}{\left(\lambda - \frac{c^2 \delta_t}{3s_7} \right)} \tag{23d}$$

$$\rho_0 \left(\partial_y w + \partial_z v \right) = \frac{G_8}{\left(\lambda - \frac{c^2 \delta_t}{3s_8} \right)} \tag{23e}$$

$$\rho_0 \left(\partial_z u + \partial_x w \right) = \frac{G_9}{\left(\lambda - \frac{c^2 \delta_t}{3s_9} \right)} \tag{23f}$$

where $G_i = \mathbf{M}_{ij} f_j - m_i^{(eq,0)} + \Psi_i / (2 - s_i)$. The above relations ensure that all quantities can be computed mesoscopically to maintain the second-order accuracy of the extended MRT.

A.2. Data post-processing details

All results in our turbulent pipe flow simulation are presented in cylindrical coordinates. The LBM results on the Cartesian grid are first transformed into cylindrical coordinates through the following binning and projection:

1. Divide the pipe cross section into 100 equal spaced bins according to their radial locations and number the bins as bin 1, 2, …, 100 from pipe center to the pipe wall. Since the pipe radius is 148.5, the bin width is 1.485 lattice units. Each lattice node is associated with a square lattice cell of width equal to one lattice unit and the node at the center. Clearly, a given lattice cell can at most overlap partially with two bins since the cell diagonal length $\sqrt{2} = 1.414$ is less than 1.485, as illustrated in Fig. 26.
2. For each square lattice cell (3D cubic lattice cell projected in 2D), identify the corner points a_0 and a_1 corresponding to the shortest and longest distances (d_0 and d_1) from the pipe centerline, respectively.
3. Find out in which bin/bins the points a_0 and a_1 are located, then one of the following cases must apply:
   (a) Both a_0 and a_1 are located in the same bin i (Fig. 26, Case 1), then add all the contribution (*i.e.*, $p(i) = 1$) from this particular cell into bin i.
   (b) a_0 is located in bin i and a_1 is located in bin $i + 1$ (Fig. 26, Case 2), then the contribution from this lattice cell is partitioned into Bin i and Bin $i + 1$, according to the following relative percentages $p(i)$ and $p(i + 1)$, respectively,

$$p(i) = \frac{l_{i,i+1} - d_0}{d_1 - d_0}, \quad p(i + 1) = \frac{d_1 - l_{i,i+1}}{d_1 - d_0}, \tag{24}$$

   where $l_{i,i+1}$ is the radial location of the boundary between bin i and bin $i + 1$. While the above is not based on the precise overlap area of the cell and a bin, but test calculations show that this partition provides a sufficiently accurate approximation compared to the true area.
   (c) a_0 is located in the last bin (Bin 100) and a_1 is located outside the pipe wall (Fig. 26, Case 3), then define $p(i)$ ($i = 100$ in this case) as
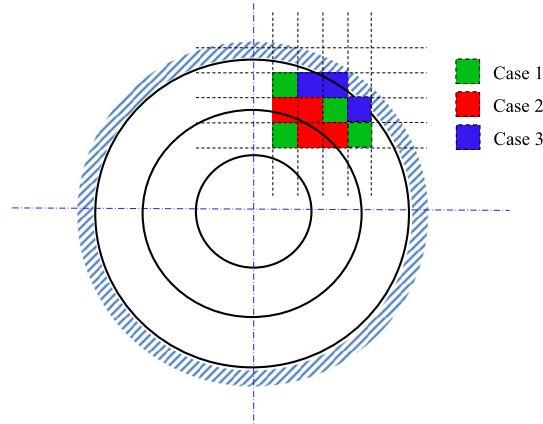
$$p(i) = \frac{R - d_0}{d_1 - d_0}. \tag{25}$$

Fig. 26. Different scenarios in the binning process of a lattice grid cell.
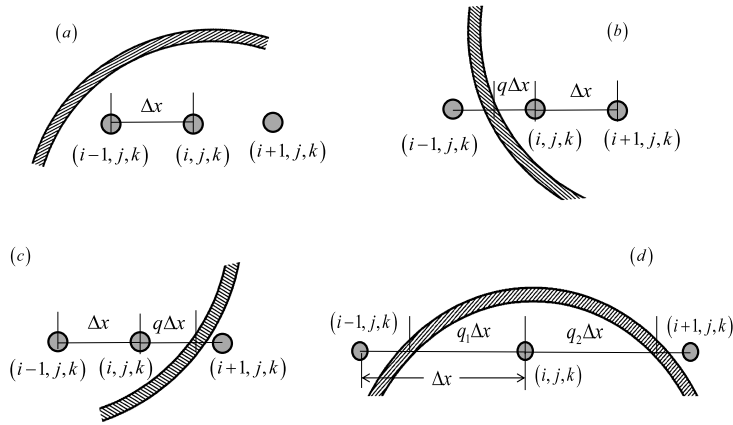

Fig. 27. Different scenarios encountered in the vorticity calculation of boundary nodes.

Each quantity is multiplied by the p value defined above, before the contribution to the bin from a particle cell is added. The average value for the bin is computed by the respective sum over all fluid cells divided by the bin volume. This post-processing strategy is applied to calculate statistical profiles. In addition to these profiles, a two-dimensional binning strategy is also presented to study the azimuthal correlations and spectra on cylindrical surfaces of different radial locations in Sec. 4.4. In azimuthal direction, each bin is evenly divided into 100 cells based on the azimuthal location of the nodes. Unlike in the radial direction where the above volumetric projection is applied, since in the azimuthal direction the flow is expected to be homogeneous, the information at each Cartesian lattice is given to the bin where the cell node is located.

A.3. Vorticity calculation

In this work, the vorticity components are calculated first in the Cartesian coordinates, and then transformed into the cylindrical coordinates. A second-order central difference scheme is applied to calculate each velocity-gradient component necessary for the calculation of vorticity components. For boundary nodes, the wall velocity is used in the situations where necessary node points for central differencing are not available. Taking $\partial u_y / \partial u_x$ as an example, there are four different situations in the vorticity calculation, as shown in (a), (b), (c) and (d) in Fig. 27. For each case, the vorticity at node (i, j, k) is calculated as follows

1. Case (a),

$$\frac{\partial u_y}{\partial x}(i, j, k) = \frac{u_y(i+1, j, k) - u_y(i-1, j, k)}{2\Delta_x} \tag{26}$$

2. Case (b),

$$\frac{\partial u_y}{\partial x}(i, j, k) = \frac{q^2 u_y(i+1, j, k) - u_{wy} + (1 - q^2) u_y(i, j, k)}{(q^2 + q)\Delta_x} \tag{27}$$

3. Case (c),

$$\frac{\partial u_y}{\partial x}(i, j, k) = -\frac{q^2 u_y (i-1, j, k) - u_{wy} + \left(1 - q^2\right) u_y (i, j, k)}{\left(q^2 + q\right) \Delta_x} \tag{28}$$

4. Case (d),

$$\frac{\partial u_y}{\partial x}(i, j, k) = (q_1 - q_2) \frac{u_{wy} - u_y (i, j, k)}{q_1 q_2 \Delta_x} \tag{29}$$

References

[1] C.K. Aidun, J.R. Clausen, Lattice-Boltzmann method for complex flows, Annu. Rev. Fluid Mech. 42 (2010) 439–472.
[2] A. ten Cate, J.J. Derksen, L.M. Portela, H.E.A. van den Akker, Fully resolved simulations of colliding mono-disperse spheres in forced isotropic turbulence, J. Fluid Mech. 519 (2004) 233–271.
[3] P. Lammers, K.N. Beronov, R. Volkert, et al., Lattice BGK direct numerical simulation of fully developed turbulence in incompressible plane channel flow, Comput. Fluids 35 (2006) 1137–1153.
[4] Y. Peng, W. Liao, L.S. Luo, et al., Comparison of the lattice Boltzmann and pseudo-spectral methods for decaying turbulence. Part I. Low-order statistics, Comput. Fluids 39 (2010) 568–591.
[5] H. Gao, H. Li, L.P. Wang, Lattice Boltzmann simulation of turbulent flow laden with finite-size particles, Comput. Math. Appl. 65 (2013) 194–210.
[6] S.K. Kang, Y.A. Hassan, The effect of lattice models within the lattice Boltzmann method in the simulation of wall-bounded turbulent flows, J. Comput. Phys. 232 (2013) 100–117.
[7] L.P. Wang, O. Ayala, H. Gao, et al., Study of forced turbulence and its modulation by finite-size solid particles using the lattice Boltzmann approach, Comput. Math. Appl. 67 (2014) 363–380.
[8] L.P. Wang, C. Peng, Z.L. Guo, Z.S. Yu, Lattice Boltzmann simulation of particle-laden turbulent channel flow, Comput. Fluids 124 (2016) 226–236.
[9] J.G.M. Eggels, F. Unger, M.H. Weiss, et al., Fully developed turbulent pipe flow: a comparison between direct numerical simulation and experiment, J. Fluid Mech. 268 (1994) 175–210.
[10] P. Loulou, R.D. Moser, N.N. Mansour, et al., Direct Numerical Simulation of Incompressible Pipe Flow Using a B-Spline Spectral Method, NASA Tech. Memo. No. 110436, 1997.
[11] C. Wagner, T.J. Huttl, R. Friedrich, Low-Reynolds-number effects derived from direct numerical simulations of turbulent pipe flow, Comput. Fluids 30 (2001) 581–590.
[12] X. Wu, P. Moin, A direct numerical simulation study on the mean velocity characteristics in turbulent pipe flow, J. Fluid Mech. 608 (2008) 81–112.
[13] C. Chin, A.S.H. Ooi, I. Marusic, et al., The influence of pipe length on turbulence statistics computed from direct numerical simulation data, Phys. Fluids 22 (2010) 115107.
[14] G.K. El Khoury, P. Schlatter, A. Noorani, P.F. Fischer, G. Brethouwer, A.V. Johansson, Direct numerical simulation of turbulent pipe flow at moderately high Reynolds numbers, Flow Turbul. Combust. 91 (3) (2013) 475–495.
[15] M. Bouzidi, M. Fordaouss, P. Lallemand, Momentum transfer of a Boltzmann-lattice fluid with boundaries, Phys. Fluids 13 (2001) 3452–3459.
[16] R. Mei, W. Shyy, D. Yu, L.S. Luo, Lattice Boltzmann method for 3-D flows with curved boundary, J. Comput. Phys. 161 (2000) 680–699.
[17] D. Yu, R. Mei, L.S. Luo, et al., Viscous flow computations with the method of lattice Boltzmann equation, Prog. Aerosp. Sci. 39 (2003) 329–367.
[18] K. Suga, Y. Kuwata, K. Takashima, et al., A D3Q27 multiple-relaxation-time lattice Boltzmann method for turbulent flows, Comput. Math. Appl. 69 (2015) 518–529.
[19] A.T. White, C.K. Chong, Rotational invariance in the three-dimensional lattice Boltzmann method is dependent on the choice of lattice, J. Comput. Phys. 230 (2011) 6367–6378.
[20] Y. Kuwata, K. Suga, Anomaly of the lattice Boltzmann methods in three-dimensional cylindrical flows, J. Comput. Phys. 280 (2015) 563–569.
[21] Z.L. Guo, H. Han, B. Shi, C. Zheng, Theory of the lattice Boltzmann equation: lattice Boltzmann model for axisymmetric flows, Phys. Rev. E 79 (2009) 046708.
[22] Q. Li, Y.L. He, G.H. Tang, W.Q. Tao, Improved axisymmetric lattice Boltzmann scheme, Phys. Rev. E 81 (2010) 056707.
[23] L. Wang, Z.L. Guo, C. Zheng, Multi-relaxation-time lattice Boltzmann model for axisymmetric flows, Comput. Fluids 39 (2011) 1542–1548.
[24] Z. Guo, T.S. Zhao, Explicit finite-difference lattice Boltzmann method for curvilinear coordinates, Phys. Rev. E 67 (2003) 066709.
[25] K. Hejranfar, E. Ezzatneshan, Implementation of a high-order compact finite-difference lattice Boltzmann method in generalized curvilinear coordinates, J. Comput. Phys. 267 (2014) 28–49.
[26] H. Xi, G. Peng, S.H. Chou, Finite-volume lattice Boltzmann method, Phys. Rev. E 56 (1999) 6202–6205.
[27] F. Dubois, P. Lallemand, On lattice Boltzmann scheme, finite volumes and boundary conditions, Prog. Comput. Fluid Dyn. 8 (2008) 11–24.
[28] Z. Guo, K. Xu, R. Wang, Discrete unified gas kinetic scheme for all Knudsen number flows: low-speed isothermal case, Phys. Rev. E 88 (3) (2013) 033305.
[29] Z. Guo, R. Wang, K. Xu, Discrete unified gas kinetic scheme for all Knudsen number flows. II. Thermal compressible case, Phys. Rev. E 91 (3) (2015) 033313.
[30] M. Min, T. Lee, A spectral-element discontinuous Galerkin lattice Boltzmann method for nearly incompressible flows, J. Comput. Phys. 230 (2011) 245–259.
[31] G. Tahitu, The Possibilities for Laser-Doppler Velocimetry in a Turbulent Pipe Flow, Report MEAH-117, Delft University of Technology, 1994, Ph.D. thesis, MSc-thesis (in Dutch).
[32] J. Westerweel, A.A. Draad, J.G.T. van der Hoeven, J. van Oord, Measurement of fully-developed turbulent pipe flow with digital particle image velocimetry, Exp. Fluids 20 (1996) 165–177.
[33] P. Lallemand, L.S. Luo, Theory of the lattice Boltzmann method: dispersion, dissipation, isotropy, Galilean invariance, and stability, Phys. Rev. E 61 (2000) 6546.
[34] D. d'Humières, I. Ginzburg, M. Krafczyk, et al., Multiple-relaxation-time lattice Boltzmann models in three-dimensions, Philos. Trans. R. Soc. A 360 (2002) 437–451.
[35] P.J. Dellar, Bulk and shear viscosities in lattice Boltzmann equations, Phys. Rev. E 64 (3) (2001) 031203.
[36] L.S. Luo, W. Liao, X. Chen, et al., Numerics of the lattice Boltzmann method: effects of collision models on the lattice Boltzmann simulations, Phys. Rev. E 83 (2011) 056710.
[37] J. Kim, P. Moin, R. Moser, Turbulence statistics in fully developed channel flow at low Reynolds number, J. Fluid Mech. 177 (1987) 133–166.
[38] G. Grötzbach, Spatial resolution requirements for direct numerical simulation of the Rayleigh–Bénard convection, J. Comput. Phys. 49 (2) (1983) 241–264.

[39] N. Geneva, C. Peng, X. Li, L.-P. Wang, A scalable interface-resolved simulation of particle-laden flow using the lattice Boltzmann method, Parallel Comput. 67 (2017) 20–37.

[40] F. Durst, J. Jovanovic, J. Sender, LDA measurements in the near-wall region of a turbulent pipe flow, J. Fluid Mech. 295 (1995) 305–335.

[41] S. Rabin, C. Caulfield, R. Kerswell, Triggering turbulence efficiently in plane Couette flow, J. Fluid Mech. 712 (2012) 244–272.

[42] C.C. Pringle, A.P. Willis, R.R. Kerswell, Minimal seeds for shear flow turbulence: using nonlinear transient growth to touch the edge of chaos, J. Fluid Mech. 702 (2012) 415–443.

[43] C. Peng, Y.H. Teng, B. Hwang, et al., Implementation issues and benchmarking of lattice Boltzmann method for moving rigid particle simulations in a viscous flow, Comput. Math. Appl. 72 (2016) 349–374.

[44] D. Kandhai, A. Koponen, A. Hoekstra, et al., Implementation aspects of 3D lattice-BGK: boundaries, accuracy, and a new fast relaxation method, J. Comput. Phys. 150 (1999) 482–501.

[45] T. Herbert, Secondary instability of boundary layers, Annu. Rev. Fluid Mech. 20 (1) (1988) 487–526.

[46] C. Peng, N. Geneva, Z. Guo, L.-P. Wang, Issues associated with Galilean invariance on a moving solid boundary in the lattice Boltzmann method, Phys. Rev. E 95 (1) (2017) 013301.

[47] T.-H. Wu, X.-M. Shao, Z.-S. Yu, Fully resolved numerical simulation of turbulent pipe flows laden with large neutrally-buoyant particles, J. Hydrodynam., Ser. B 23 (1) (2011) 21–25.

[48] X. He, L.-S. Luo, Lattice Boltzmann model for the incompressible Navier–Stokes equation, J. Stat. Phys. 88 (3–4) (1997) 927–944.

[49] H.D. Min, C. Peng, Z.L. Guo, L.P. Wang, An inverse design analysis of mesoscopic implementation of non-uniform forcing in MRT lattice Boltzmann models, Comput. Math. Appl. (2016), https://doi.org/10.1016/j.camwa.2016.04.040, in press.

[50] T. Inamuro, A lattice kinetic scheme for incompressible viscous flows with heat transfer, Philos. Trans. R. Soc. A 360 (2002) 477–484.

[51] L.-P. Wang, H. Min, C. Peng, N. Geneva, Z. Guo, A lattice-Boltzmann scheme of the Navier–Stokes equation on a three-dimensional cuboid lattice, Comput. Math. Appl. (2016), https://doi.org/10.1016/j.camwa.2016.06.017, in press.